Uncertainty-bounded estimates of ash cloud properties using the ORAC algorithm: Application to the 2019 Raikoke eruption

Andrew T. Prata[1], Roy G. Grainger[1], Isabelle A. Taylor[2], Adam C. Povey[3], Simon R. Proud[3,4], and Caroline A. Poulsen[5]

[1]Atmospheric, Oceanic and Planetary Physics, University of Oxford, Oxford OX1 3PU, UK
[2]COMET, Atmospheric, Oceanic and Planetary Physics, University of Oxford, Oxford OX1 3PU, UK
[3]National Centre for Earth Observation, Atmospheric, Oceanic and Planetary Physics, University of Oxford, Oxford OX1 3PU, UK
[4]RAL Space, STFC Rutherford Appleton Laboratory, Harwell Campus, Didcot OX11 0QX, UK
[5]Australian Bureau of Meteorology, Melbourne, Australia

Correspondence: Andrew Prata (andrew.prata@physics.ox.ac.uk)

Abstract. Uncertainty-bounded satellite retrievals of volcanic ash cloud properties such as ash cloud-top height, effective radius, optical depth and mass loading are needed for the robust quantitative assessment required to warn aviation of potential hazards. Moreover, there is an imperative to improve quantitative ash cloud estimation due to the planned move towards quantitative ash concentration forecasts by the Volcanic Ash Advisory Centers. Here we apply the Optimal Retrieval of Aerosol and Cloud (ORAC) algorithm to Advanced Himawari Imager (AHI) measurements of the ash clouds produced by the June 2019 Raikoke (Russia) eruption. The ORAC algorithm uses optimal estimation to consolidate *a priori* information, satellite measurements and associated uncertainties into uncertainty-bounded estimates of the desired state variables. Using ORAC, we demonstrate several improvements in thermal infrared volcanic ash retrievals applied to broadband imagers. These include: an improved treatment of measurement noise, accounting for multi-layer cloud scenarios, distinguishing between heights in the troposphere and stratosphere, and the retrieval of a wider range of effective radii sizes than existing techniques by exploiting information from the 10.4 μm channel. Our results indicate that 0.73 ± 0.40 Tg of very fine ash (≤ 15 μm, radius) was injected into the troposphere and stratosphere during the main eruptive period from 21 June 18:00 UTC to 22 June 10:00 UTC. The total mass of very fine ash decreased from 0.73 Tg to 0.10 Tg over ~48 h with an e-folding time of 20 h. We also estimate a distal fine ash mass fraction of 0.47 ± 0.37 % based on the total mass of very fine ash retrieved and the ORAC-derived height time-series. Several distinct ash layers were revealed by the ORAC height retrievals. Generally, ash in the troposphere was composed of larger particles than ash present in the stratosphere. We also find that our implementation of the ORAC algorithm was reliable out to four days and was able to track the median ash cloud at concentrations below peak ash concentration safety limits (<4 mg m^{-3}) if typical ash cloud geometric thicknesses were assumed. The ORAC height retrievals for the Raikoke case study have a bias and precision of -2.22 km and 2.85 km, respectively, based on comparisons with CALIOP and GOES-17 height validation data. The dataset generated here provides uncertainties at the pixel level for all retrieved variables and could potentially be used for dispersion model validation or implemented in data assimilation schemes. Future work should focus on

improving ash detection, improving height estimation in the stratosphere and exploring the added benefit of visible channels for retrieving effective radius and optical depth in opaque regions of nascent ash plumes.

1 Introduction

25 Volcanic Ash Advisory Centers (VAACs) require satellite observations to detect and track volcanic ash clouds that pose a threat to aviation. In addition to detection and tracking, VAACs use dispersion models to forecast the position of a volcanic ash cloud. Currently, VAACs are required to provide qualitative, deterministic forecasts indicating the future position of potentially hazardous ash clouds and satellite detection schemes have been developed in support of this operational requirement (Pavolonis et al., 2015b, a). However, according to the International Airways Volcano Watch (IAVW) roadmap, by 2025, VAACs will be

30 required to issue quantitative forecasts of ash concentration (ICAO, 2019). The move to quantitative dispersion model forecasts motivates the need for validation to improve the overall quality of the forecast. The thermal infrared (IR) capabilities of the current generation of geostationary satellite sensors are particularly well suited to this purpose as they offer continuous, day and night observations at finer spatial (2 km) and temporal (10 minute) resolutions than operational dispersion model output grids (typically 10–25 km and 1–3 h). Thermal IR geostationary satellite observations are useful for quantitative validation

35 (Wilkins et al., 2016; Prata et al., 2021; Folch et al., 2022), source term characterisation (Pouget et al., 2013; Van Eaton et al., 2016; Prata et al., 2020), data insertion (Wilkins et al., 2015, 2016; Folch et al., 2020; Prata et al., 2021), data assimilation (Lu et al., 2016; Pardini et al., 2020; Zidikheri and Lucas, 2021; Mingari et al., 2022) and source term inversion (Stohl et al., 2011; Harvey et al., 2020, 2022). In addition, it is important that uncertainties in satellite retrievals are accurately characterised because the VAACs and other users of satellite retrievals increasingly require uncertainty information to correctly interpret,

40 aggregate and utilise the data.

Volcanic ash retrievals from satellite data are possible in the thermal IR because of the high SiO_2 content of volcanic ash, which has a strong absorption feature around the 9.5 μm wavelength region (Soda, 1961; Grainger et al., 2013; Prata et al., 2019). Volcanic ash clouds can be discriminated from ice and water clouds as their absorption properties act in opposite directions across the thermal IR window, a property known as the 'reverse absorption' effect (Prata, 1989a, b). Wen and Rose

45 (1994) and Prata and Grant (2001) demonstrated how estimates of the effective radius and optical depth could be obtained on the basis of two split-window brightness temperature measurements centred near 11 and 12 μm. Based on this principle, mass loadings (mass per unit area) can be derived at pixel-scale resolution and when combined with vertical profile information, ash concentrations can be estimated (Prata and Prata, 2012).

Uncertainties in satellite-based, ash cloud retrieval algorithms are dominated by inaccuracies in the physical model whereby

50 ash cloud properties or 'state variables' (such as cloud-top pressure or height, optical depth and effective radius) are converted into satellite-measured radiances. This is achieved using a radiative transfer forward model (FM) which simulates top-of-the-atmosphere (TOA) radiances based on certain assumptions about the atmospheric state. Numerous simplifying assumptions are needed to evaluate the FM and each of these assumptions introduce FM uncertainty. Examples include: parameterising a cloud layer in terms of its microphysical, optical and geometric properties; assuming whether or not it is plane-parallel (i.e.

55 neglecting 3D radiative effects); parameterising the underlying surface characteristics. Additional uncertainties arise due to uncertainty in ancillary information, often derived from reanalysis data derived from Numerical Weather Prediction (NWP) models, such as profiles of temperature, humidity and trace gases. Uncertainties related to the measurements must also be considered, which include channel noise and co-registration as well as scene-dependent uncertainties introduced by sub-pixel scale inhomogeneity.

60 Uncertainty in the total mass of very fine ash (≤ 15 µm, radius) derived using the split-window method has been estimated from sensitivity analyses and is generally found to be 40–60% (Wen and Rose, 1994; Gu et al., 2003; Corradini et al., 2008; Prata and Prata, 2012; Prata et al., 2017b). Sources of FM uncertainty that have previously been considered include the assumed ash composition (e.g. Wen and Rose, 1994; Mackie et al., 2014), form of the underlying size distribution (e.g. Wen and Rose, 1994; Western et al., 2015), variation in surface and cloud-top temperature (e.g. Corradini et al., 2008; Schneider et al., 1999),

65 particle shape (Kylling et al., 2014) and meteorological cloud interference (Kylling et al., 2015). While broad estimates of uncertainty in the total mass of very fine ash are useful, it is desirable to have pixel-scale, uncertainty-bounded estimates of all retrieved quantities.

 Optimal estimation (OE; Rodgers, 1976, 2000) is particularly useful for solving the noisy inverse problem where imperfect prior knowledge in the state space is quantified in terms of probability density functions (PDFs) and noise in the measurements

70 is quantified in terms of PDFs in the measurement space. Within the OE framework, one can assume large uncertainties on the priors such that the solution is influenced mainly by the measurements or set small uncertainties if good quality *a priori* information is available. Optimal estimation also provides a formalism where state and measurement variables can be easily added or removed and uncertainties in prior information and the measurements are propagated through the FM equations to estimate uncertainties in all retrieved state variables.

75 There are several examples of OE-retrievals that use thermal-only measurements of volcanic ash, each using different state variables and instrument channels but all aiming to retrieve the ash mass loading and cloud-top height. For example, the Pavolonis et al. (2013) algorithm, used by the Washington, Anchorage and Darwin VAACs, includes the effective cloud temperature, effective cloud emissivity (at 11 µm) and the 'β-ratio' (the ratio of effective optical depth at 12 and 11 µm) in the state vector. From these state variables, cloud-top height and mass loading are derived. The measurement vector used by Pavolonis

80 et al. (2013) includes the 11 µm brightness temperature and two brightness temperature differences (BTDs; 11-12 µm and 11-13.3 µm). Uncertainties considered by Pavolonis et al. (2013) include measurement (instrument) error, clear-sky radiance errors (land and water are treated separately) and spatial heterogeneity errors. For the measurement errors in each channel, a fixed, noise-equivalent delta temperature (NEΔT), as reported by the satellite provider, is used. The Francis et al. (2012) algorithm, used by the London VAAC, includes the effective radius, cloud-top pressure and mass loading in their state vector and use

85 the 11, 12 and 13.3 µm brightness temperatures in their measurement vector. Similar to Pavolonis et al. (2013), Francis et al. (2012) also use fixed NEΔT values to estimate measurement uncertainty for each channel included in the measurement vector while FM uncertainty is estimated using statistics derived from long-term, cloud-free satellite radiances. Kylling et al. (2015) present a simple OE scheme that retrieves two state variables (effective radius and optical depth) based on two measurements (11 and 12 µm brightness temperatures) from which mass loading is computed. Cloud-top height is not provided in their paper,

but could have been inferred from their estimation of cloud-top temperature using a nearby meteorological temperature profile (from a NWP model or sounding). To characterise uncertainty in their retrieval, Kylling et al. (2015) use the combined (FM and measurement) uncertainties provided in Francis et al. (2012).

A common theme amongst existing retrieval schemes is the use of a fixed measurement error (i.e. NEΔT) per channel. However, this noise estimate is only true for the reference temperature given. It is straightforward to allow NEΔT to vary based on the measured brightness temperature and we highlight this improvement in the present study (Sect. 3.2.2). Another key result from the work of Pavolonis et al. (2013) and Francis et al. (2012) is that the inclusion of the 13.3 μm channel enables good estimates of ash cloud-top height, as shown by validation with the Cloud-Aerosol Lidar and Infrared Pathfinder Satellite Observation (CALIPSO) satellite lidar measurements presented in their studies. As we will show, the 13.3 μm channel is key for distinguishing between ash clouds in the troposphere and stratosphere. Additionally, no authors have yet published an ash OE-scheme that incorporates the 10.4 μm channel in addition to channels centred near 11, 12 and 13.3 μm. The 10.4 μm channel is a window channel less affected by water vapour than the 11 μm and 12 μm channels (Lindsey et al., 2012) and is positioned closer to the 9.5 μm silica absorption band.

We focus on quantifying ash cloud properties and their associated uncertainties using the Optimal Retrieval of Aerosol and Cloud (ORAC) algorithm applied to Advanced Himawari Imager (AHI) observations using the June 2019 Raikoke (Russia) eruption as a case study. The main aim of this study is to provide uncertainty-bounded estimates of optical depth, effective radius, cloud-top height and mass loading for the Raikoke ash clouds, while simultaneously describing new advances in thermal-only volcanic ash retrievals applied to satellite imager instruments using an OE framework. Specifically, we present a time-series of the Raikoke ash cloud properties and discuss our results in the context of existing studies on Raikoke. We present a new method for quantifying ash cloud heights in the troposphere and stratosphere (a common feature of explosive volcanic eruptions such as Raikoke). We also present the first ash retrievals for the Raikoke case which consider multi-layered cloud (ash over water cloud) and present a technique for selecting the best-fitting FM based on measurement cost at solution. We consider uncertainty variation in measured brightness temperatures which advances previous methods of assuming constant brightness temperature errors. Finally, we explore the advantages of using the 10.4 μm channel in OE retrievals of volcanic ash and demonstrate that its inclusion enables the retrieval of a wider range of effective radii sizes.

2 Data

2.1 Advanced Himawari Imager

The Advanced Himawari Imager (AHI) aboard the Japanese Meteorological Agency's (JMA) Himawari-8 satellite has been in operation since 7 July 2015. The AHI is in geostationary orbit nominally positioned at 140.7° E and completes a full disk scan every ten minutes (Bessho et al., 2016). The AHI has sixteen spectral bands with spatial resolutions at nadir of 0.5 km (band 3), 1 km (bands 1, 2 and 4) and 2 km (bands 5–16). The ORAC algorithm has been applied to level 1b Himawari Standard Data (HSD) files, which contain radiances that have been sampled onto the World Geodetic System 1984 (WGS84) ellipsoid. The radiances were converted to brightness temperatures using the JMA's standard calibration (calibration information block 5 of

the header). A subset of the AHI full disk defined by 40–65° N and 135–195° E has been analysed from 18:00 UTC on 21 June 2019 to 18:00 UTC on 28 June 2019. This corresponding to one week of observations from eruption onset.

2.2 Advanced Baseline Imager

To validate ORAC-AHI retrievals of cloud-top height in the near-source volcanic plume we use the recently published dataset from Horváth et al. (2021a, b) who provide geometric estimations of plume-top height. Specifically, we use the GOES-17 Advanced Baseline Imager (ABI) 'side view' height estimations provided in the Supplementary Material in Horváth et al. (2021a). Uncertainty on these height retrievals is ± 500 m.

2.3 CALIOP

To validate the ORAC-AHI retrievals of cloud-top height for distal ash clouds, we use the level 2 lidar products generated from measurements made by the Cloud-Aerosol Lidar with Orthoganol Polarisation (CALIOP) aboard the CALIPSO platform (Winker et al., 2009). The level 2 version 4.20, 5 km combined cloud and aerosol layer product (L2_05kmMLay-Standard-V4-20) is used to extract ash cloud heights and geometric thicknesses for validation purposes. The precision with which CALIOP measures layer top and base height varies with altitude. From -0.5 km to $\sim$ 8.2 km, the vertical resolution is 30 m and from $\sim$ 8.2 km to $\sim$ 20.2 km, the vertical resolution is 60 m.

3 Method

3.1 Forward model

The ORAC algorithm is an open source software initially developed by the University of Oxford and Rutherford Appleton Laboratory (RAL). The Deutscher Wetterdienst (DWD) have developed the code alongside Oxford and RAL since 2010. The Australian Bureau of Meteorology is also a contributor. Within ORAC two distinct FM implementations are available to retrieve aerosol or cloud properties (or combined for a joint retrieval). Details of the aerosol FM are provided in Thomas et al. (2009) and the cloud FM details can be found in Poulsen et al. (2012) and McGarragh et al. (2018). For volcanic ash we use the ORAC FM equations for cloud, so no details for the aerosol FM equations are given here. In the cloud model, the solar and thermal components of terrestrial radiation are considered separately, but are minimised simultaneously. As we only use thermal channels in our measurement vector, we focus on the thermal FM within ORAC.

The top-of-the-atmosphere radiance (L_{TOA}), measured by a downward-looking satellite, for a plane-parallel cloud at thermal wavelengths (3–15 μm) can be written as (McGarragh et al., 2018)

$$L_{\mathrm{TOA}} = L_{\mathrm{ac}}^{\uparrow} + [L_{\mathrm{ac}}^{\downarrow} R_{\mathrm{db}}^{\uparrow}(\theta_v) + B(T_{\mathrm{c}})\epsilon(\theta_v) + L_{\mathrm{bc}}^{\uparrow} t_{\mathrm{db}}^{\uparrow}(\theta_v)] t_{\mathrm{ac}}^{\uparrow}(\theta_v), \qquad (1)$$

where $L_{\mathrm{ac}}^{\uparrow}$ is the above cloud upwelling radiance, $L_{\mathrm{ac}}^{\downarrow}$ is the above cloud downwelling radiance, $R_{\mathrm{db}}^{\uparrow}(\theta_v)$ is the portion of above cloud, downwelling radiance reflected towards the viewing direction of the satellite, θ_v, $B(T_{\mathrm{c}})$ is the Planck radiance at the

cloud-top temperature, T_c, $\epsilon(\theta_v)$ is the cloud emissivity, $L_{bc}^\uparrow$ is the below cloud upwelling radiance, $t_{db}^\uparrow(\theta_v)$ is the upward diffuse transmittance of the cloud and $t_{ac}(\theta_v)$ is the above cloud transmittance of the atmosphere. Note that if we assume that the reflected portion of above cloud, downwelling thermal radiance is negligible (i.e. $L_{ac}^\downarrow R_{db}^\uparrow \approx 0$) and recognise that $t_{db}^\uparrow(\theta_v) = 1 - \epsilon(\theta_v)$ then Eq. 1 reduces to the FM formulations used in Pavolonis et al. (2013) and Francis et al. (2012):

$$L_{\mathrm{TOA}} = \epsilon L_{\mathrm{cld}} + (1 - \epsilon) L_{\mathrm{clr}}, \tag{2}$$

where

$$L_{\mathrm{clr}} = L_{bc}^\uparrow t_{ac} + L_{ac}^\uparrow \tag{3}$$

and

$$L_{\mathrm{cld}} = L_{ac}^\uparrow + B(T_c) t_{ac}. \tag{4}$$

Further, if it is assumed that the atmosphere is perfectly transparent and the surface has an emissivity of 1, then $L_{\mathrm{clr}} = B(T_s)$ and $L_{\mathrm{cld}} = B(T_c)$ and we arrive at the original formulation proposed by Prata (1989a) (i.e. $L_{\mathrm{TOA}} \approx \epsilon B(T_c) + (1 - \epsilon) B(T_s)$). Therefore, although there are significant differences in the practical implementation of the ORAC thermal FM and those of Pavolonis et al. (2013) and Francis et al. (2012), the main difference in its theoretical formulation is the inclusion of non-zero above cloud reflectance of downwelling radiance (as written in Eq. 1). Another important difference is that we include surface temperature, T_s, in the state vector. This means that $L_{bc}^\uparrow$ must be updated during the retrieval process. For computational efficiency $L_{bc}^\uparrow$ is written as a linear expansion in temperature (McGarragh et al., 2018):

$$L_{bc}^\uparrow = L_{bc,a}^\uparrow + (T_s - T_{s,a}) \frac{\partial L_{bc,a}^\uparrow}{\partial T_{s,a}} \epsilon_s t_{bc}(\theta_v), \tag{5}$$

where $T_{s,a}$ is the *a priori* surface temperature (taken from NWP data), ϵ_s is the emissivity of the surface and $t_{bc}(\theta_v)$ is the transmittance from the surface to the cloud layer. The clear-sky radiance and transmittance terms are computed using version 13 of RTTOV (Radiative Transfer for TOVS; Saunders et al., 2018). As a pre-processing task, RTTOV is run on atmospheric profiles of temperature, specific humidity and ozone taken from ERA5 reanalysis data (Hersbach et al., 2020). The ERA5 data are interpolarted in time to match the satellite observation time from a $0.5° \times 0.5°$ global grid at 6 h temporal resolution. Clear-sky, above cloud and below cloud transmittance and radiance profiles are then passed to ORAC. A cloud layer is inserted into the FM by interpolating the above and below radiance and transmittance profiles to the first guess pressure of the state vector. The cloud layer is assumed to be a geometrically (but not optically) infinitesimal layer (McGarragh et al., 2018). This implementation is fast and flexible because once the pre-processing task is done, any cloud optical properties can be introduced or modified. In addition, this approach allows for both single and multi-layer FM configurations and delegates the generation of computationally expensive single-scattering cloud properties to offline calculations.

The single-scattering properties for the cloud layer are generated as look-up tables (LUTs) using version 2.1 of DISORT (Stamnes et al., 2000). Volcanic ash LUTs are generated as a function of the 550 nm optical depth, τ (17 grid points from

0–256 with $\log_{10}$ spacing), effective radius, r_e (13 grid points at 0.1 μm, 0.5 μm and 1–15 μm in 1 μm intervals), θ_v (10 grid points from 0–90° in 10° intervals) and λ (convolved to the relevant channel spectral response function). Ash composition information is accounted for using complex refractive index data taken from the Oxford Aerosol Refractive Index Archive
185 (ARIA, http://eodg.atm.ox.ac.uk/ARIA/). As we do not have refractive index data for the Raikoke ash, we ran the retrieval with three different types of ash (with varying silica content), reported by Reed et al. (2018), that were sampled from the 2010 Eyjafjallajökull (Iceland) eruption, 1981 Mt Spurr (Alaska, USA) eruption and 2008 Chaitén (Chile) eruption. However, after running the ORAC retrieval for all three ash compositions, we found that the Eyjafjallajökull ash consistently outperformed the other two ash compositions (i.e. lower cost and more retrievals converging). We therefore present retrieval results only for the
190 Eyjafjallajökull ash composition. Particles were assumed spherical and the underlying size distribution was assumed to follow a lognormal distribution with a spread of 2.

ORAC currently allows for the inclusion of two cloud layers in the FM. As there was prevalent stratus cloud during the Raikoke eruption we ran ORAC in both single-layer and multi-layer mode. In multi-layer mode we tried two FM configurations: one with a tightly constrained, low-level (800 hPa) water layer underlying an ash layer and the second with a tightly constrained,
195 mid-level (500 hPa) water cloud underlying an ash layer. We also varied *a priori* settings for the single and multi-layer runs (described in Sect. 3.2.3).

3.2 Optimal estimation

The OE technique implemented in ORAC utilises Bayes' theorem so that uncertainties in *a priori* information can be considered in addition to uncertainties (noise) in the satellite measurements (Rodgers, 2000). In practice, the goal of OE is to minimise a
200 cost function that is described by a χ^2 distribution:

$$\chi^2 = [\mathbf{y} - \mathbf{F}(\mathbf{x}, \mathbf{b})]^T \mathbf{S}_\epsilon^{-1} [\mathbf{y} - \mathbf{F}(\mathbf{x}, \mathbf{b})] + [\mathbf{x} - \mathbf{x_a}]^T \mathbf{S_a}^{-1} [\mathbf{x} - \mathbf{x_a}], \tag{6}$$

where $\mathbf{y}$, $\mathbf{x}$ and $\mathbf{x_a}$ are the measurement, state and *a priori* state vectors, respectively, $\mathbf{F}(\mathbf{x}, \mathbf{b})$ is the FM vector (i.e. Eq. 1 converted to brightness temperatures for each satellite channel), which is a function of ancillary information, $\mathbf{b}$, as well as $\mathbf{x}$. Forward model and measurement uncertainties are contained in the measurement error covariance matrix, $\mathbf{S}_\epsilon$, and *a priori*
205 uncertainties are contained in the *a priori* error covariance matrix, $\mathbf{S_a}$. Here it is worth noting that $\mathbf{S}_\epsilon$ and $\mathbf{S_a}$ are assumed diagonal and so all off-diagonal elements (i.e. the covariances) are zero. Therefore, when making this assumption one should be careful to select state variables that are independent of each other. To minimise Eq. 6, the ORAC algorithm uses the well-known Levenberg–Marquardt minimisation scheme (Levenberg, 1944; Marquardt, 1963). Details regarding the implementation of Levenberg–Marquardt for the present study are provided in McGarragh et al. (2018).

3.2.1 State and measurement vectors

When constructing state and measurement vectors it is important to consider whether or not the measurements contain enough information about the state that is being retrieved. It is therefore good practice to use at least as many independent measurements as there are state variables. The ORAC state vector contains five state variables: optical depth (τ), effective radius (r_e), cloud-

top pressure (p_c), surface temperature (T_s) and cloud fraction (f). However, here we do not attempt to retrieve f and assume it

215 is always equal to one. Thus the state vector used for the ash retrievals presented here contains four state variables:

$$
\mathbf{x} = \begin{pmatrix} \log_{10}(\tau) \\ r_e \\ p_c \\ T_s \end{pmatrix}.
\tag{7}
$$

Early studies on volcanic ash clouds (e.g. Prata, 1989a; Wen and Rose, 1994; Prata and Grant, 2001) have shown that for a

given T_s and T_c, r_e varies with the 11-12 μm BTD and τ varies with brightness temperature measured at 11 μm (or 12 μm).

The dependence of r_e on the BTD has also been shown for semi-transparent ice and water clouds (Inoue, 1985; Yamanouchi

220 et al., 1987; Prabhakara et al., 1988; Parol et al., 1991; Key, 1995; Cooper et al., 2006; Wang et al., 2011). This explains why

OE schemes attempting to retrieve r_e and τ from thermal-only measurements often include window channels centred near 11

and 12 μm in the measurement vector. Further, as discussed in Pavolonis et al. (2013) and Francis et al. (2012), the addition of

the 13.3 μm to the measurement vector improves cloud-top pressure (height) estimation, particularly for optically thin, upper-

troposphere/lower-stratosphere (UTLS) ash clouds and the same applies to cirrus clouds (Heidinger et al., 2010). Channels

225 centred near 10.4 μm aboard geostationary imagers (e.g. ABI and AHI) have only recently become available and it is thought

that with the inclusion of the 10.4 μm channel to the measurement vector, additional microphysical information on volcanic

ash particles may be extracted (Pavolonis and Sieglaff, 2012; Pavolonis et al., 2020). We therefore include AHI channels 10.4,

11.2, 12.4 and 13.3 μm in our measurement vector so that

$$
\mathbf{y} = \begin{pmatrix} T_{10} \\ T_{11} \\ T_{12} \\ T_{13} \end{pmatrix},
\tag{8}
$$

230 where $T_{10}, T_{11}, T_{12}, T_{13}$ represent the brightness temperatures in the 10.4, 11.2, 12.4 and 13.3 μm AHI channels, respectively.

These channels are advantageous not just for the reasons mentioned above but also because they are unaffected by SO_2 ab-

sorption, which is not currently included in our FM and was present in abundance for the Raikoke case (Hyman and Pavolonis,

2020; Prata et al., 2021; de Leeuw et al., 2021).

3.2.2 Forward model and measurement uncertainty

235 Forward model uncertainties arise due to assumptions and approximations used to evaluate the FM. Based on previous studies

with earlier versions of the ORAC algorithm (Watts et al., 1998, 2011; Poulsen et al., 2012), we assume fixed uncertainty in the

thermal channels of 0.50 K which accounts for uncertainties due to the plane-parallel assumption (i.e. 3D radiative effects) and

sub-pixel scale inhomogeneity (Iwabuchi and Hayasaka, 2002). We also account for errors due to misalignment (co-registration

errors) between channels assuming a fixed uncertainty of 0.15 K for each channel.

To estimate measurement uncertainties in thermal infrared channels, we use the noise-equivalent delta temperature (NEΔT). As mentioned earlier, the NEΔT for satellite imager channels is reported at a particular reference temperature (T_0) and thus it is only accurate for that reference temperature. However, it is straightforward to allow error in the measurements to vary with the measured brightness temperature, which recognises that increased signal (i.e. higher brightness temperatures) will result in reduced noise and vice-versa. We therefore compute measurement noise (δT_m) for each channel based on the measured brightness temperature per pixel as follows

$$\delta T_m = \delta T_0 \left(\frac{\partial B(T_0)}{\partial T_0} \bigg/ \frac{\partial B(T_m)}{\partial T_m} \right), \tag{9}$$

where δT_0 is the NEΔT reported by the satellite instrument provider and $B(T_0)$ and $B(T_m)$ are Planck functions evaluated at T_0 and T_m. Figure 1 shows how Eq. 9 allows the measurement noise to vary for a range of brightness temperatures for each channel used in our measurement vector. For reference, the NEΔT for each channel is plotted as a horizontal dashed line to demonstrate how uncertainties using a fixed value lead to underestimations of uncertainty for colder brightness temperatures.

3.2.3   Lowest cost, a priori settings and first guess

One of the advantages of the ORAC algorithm is that it allows the user to easily modify cloud layer properties for both single layer and multi-layer FM configurations. Given that there were numerous meteorological clouds (at low- to mid-tropospheric levels) underlying the Raikoke ash clouds, we considered both single-layer ash and multi-layer (ash over water cloud) scenarios. A further consideration was how to deal with local vs. global minima in the cost surface. Considering that the Raikoke ash dispersed into the troposphere and stratosphere (Muser et al., 2020; Horváth et al., 2021b) and that we use thermal-only channels in our retrieval, the height retrievals are strongly-dependent on the temperature profile. Therefore, retrieving heights in the troposphere and stratosphere pose the potential problem of a multiple solutions (or multiple minima in the cost surface) due to the inversion of temperature at the tropopause. An additional complication is in the case of an isothermal region in the atmosphere (or a flat cost surface) which is fairly typical of the lower-stratosphere at high latitudes. A nearby radiosonde sounding at around the time of the Raikoke eruption illustrates the problem (Fig. 2).

To address issues related to the retrieval of cloud-top pressure, we ran ORAC using five different configurations representing different choices of the *a priori* pressures in the single and multi-layer FMs. The *a priori* pressure settings were chosen based on CALIPSO observations at the beginning of the eruption (see Prata et al., 2021, Fig. B3(a)) and are summarised in Table 1. For retrieval configurations with a tropospheric, *a priori* ash layer pressure, the first guess was set to the pressure level where the measured T_{11} brightness temperature was closest to the ERA5 temperature (searching from the surface to the top-of-atmosphere). For ash layers with an *a priori* pressure level in the stratosphere, the first guess was set equal to the *a priori*. The ash layer *a priori* for τ was set to 0.5, which is a typical of value for ash cloud retrievals reported in the literature (e.g. Corradini et al., 2016). For the ash layer *a priori* effective radius, we set r_e to 5 μm, which corresponds roughly to the centre of particle sensitivity for thermal IR channels (Prata and Grant, 2001). The ash layer *a priori* uncertainties on τ and r_e were set to 10^8, meaning that these parameters were effectively unconstrained by their *a priori* values. The *a priori* values for τ and r_e for water cloud were chosen based on ORAC cloud retrievals (Poulsen et al., 2012; McGarragh et al., 2018) applied to a
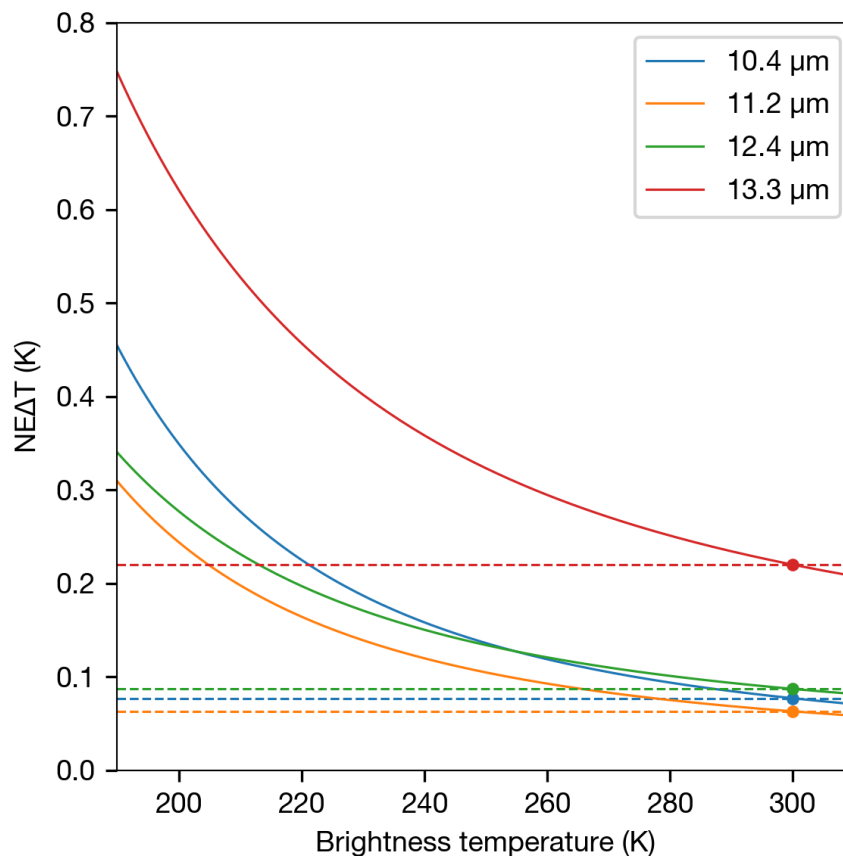
Figure 1. Relationship between fixed noise uncertainty values (dashed lines) and varying uncertainty noise values (solid lines) derived from Eq. 9. Solid circles indicate reference temperatures (T_0) given for the NEΔT estimate.

stratus deck close to the ash cloud at the beginning of the Raikoke eruption. The water layer *a priori* uncertainties for p_c, τ and r_e were tightly constrained such that the measurements only influenced the solution for the upper ash layer in the multi-layer runs. The *a priori* settings for τ, r_e and T_s are summarised in Table 2.

After all five retrieval configurations were run, the retrieval configuration which resulted in the lowest cost was selected on a per-pixel basis to generate the final retrieval product. In summary, this approach accounts for multi-layer cloud scenarios, multiple local minima in the cost function (in the troposphere and stratosphere) and reduces the impact of flat cost surfaces (isothermal regions) with the use of the *a priori* uncertainty settings.
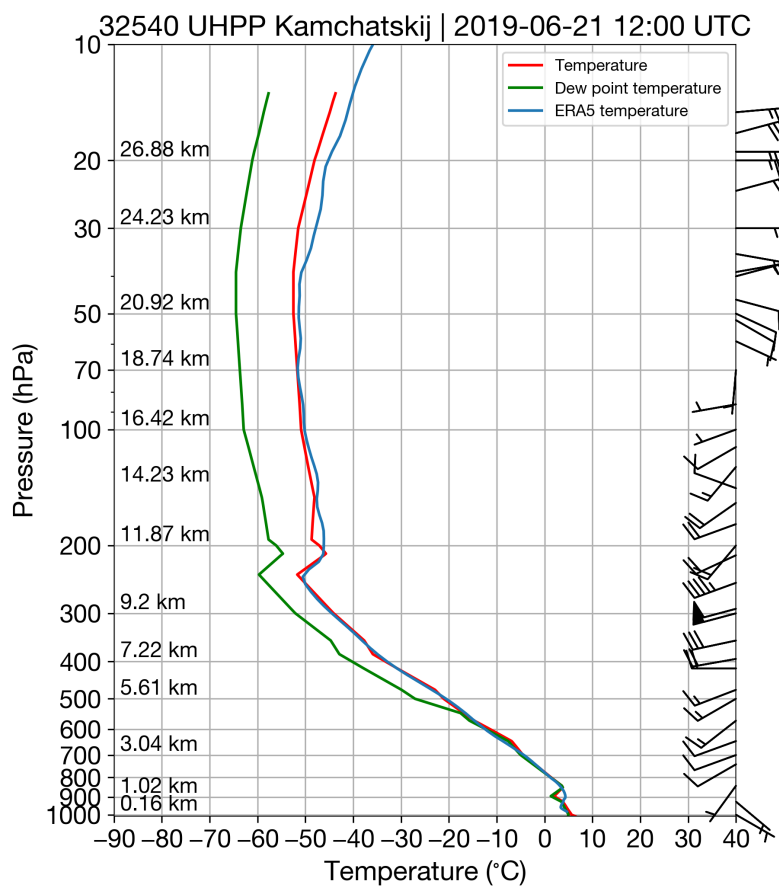
Figure 2. Radiosonde sounding from Kamchatskij station (53.08° N, 158.58° E, 84 m) at 12:00 UTC on 21 June 2019. Data accessed from University of Wyoming sounding database (last access 26 February 2022). ERA5 temperature for the grid-box corresponding to Kamchatskij station's location and sounding time is over-plotted in blue.

3.3 Ash mass loading and uncertainty

To compute ash mass loading (mass per unit area) we use the standard formulation used by many previous authors (Wen and Rose, 1994; Prata and Grant, 2001; Corradini et al., 2008; Pavolonis et al., 2013):

$$m_l = \frac{4}{3} \times \frac{\tau \cdot r_e \cdot \rho}{Q_{\text{ext}}}, \tag{10}$$

where τ is the optical depth at 550 nm, Q_{ext} is the extinction efficiency factor for ash at 550 nm ($Q_{\text{ext}} \approx 2$ at 550 nm) and ρ is the ash particle density, assumed to be 2300 kg m^{-1}. It is interesting to note that the definition of ash mass loading is analogous to the cloud liquid-water path found in numerous cloud retrieval studies (see Eq. 24 of Poulsen et al., 2012, for example). To compute uncertainty on the ash mass loading, Δm_l, we assume all variables are independent and sum the error

Table 1. *A priori* and first guess settings for p_c for both multi-layer and single layer forward model configurations. Lower and upper limits within ORAC for p_c are 10 hPa and 1200 hPa, respectively.

Forward model	*A priori*	First guess	Uncertainty
Ash single layer	500 hPa	ERA5	200 hPa
Ash single layer	200 hPa	200 hPa	200 hPa
Ash above water	500 hPa / 800 hPa	ERA5 / 800 hPa	200 hPa / 50 hPa
Ash above water	200 hPa / 800 hPa	200 hPa / 800 hPa	100 hPa / 50 hPa
Ash above water	200 hPa / 500 hPa	200 hPa / 500 hPa	100 hPa / 50 hPa

Table 2. *A priori* settings for τ, r_e and T_s for the ash and water layers considered. All first guesses for these parameters were set to be equal to their *a priori* values.

Parameter	τ_{ash}	$r_{e,\mathrm{ash}}$ (μm)	τ_{wat}	$r_{e,\mathrm{wat}}$ (μm)	T_s (K) (sea/land)
A priori	0.5	5	16	10	ERA5
Uncertainty	1×10^8	1×10^8	2	1	2.0/5.0
Lower limit	0.001	0.01	0.001	0.1	200
Upper limit	255.9	20	255.9	35	400

terms in quadrature:

$$\left(\frac{\Delta m_l}{m_l}\right)^2 = \left(\frac{\Delta \tau}{\tau}\right)^2 + \left(\frac{\Delta r_e}{r_e}\right)^2 + \left(\frac{\Delta \rho}{\rho}\right)^2 + \left(\frac{\Delta Q_{\mathrm{ext}}}{Q_{\mathrm{ext}}}\right)^2. \tag{11}$$

290   Note here all error terms are retrieved, except for the ash particle density, $\Delta \rho$, which is assumed to have an absolute uncertainty of 300 $\mathrm{kg\,m^{-1}}$, and ΔQ_{ext}, which is assumed to be negligible compared to the other error terms.

3.4 Ash detection flag

By default ORAC is run on every level 1b satellite pixel in the full disk image. In some circumstances retrievals can converge, albeit with a poor fit to the measurements (high cost), even when the FM is not representative of the observation. To avoid these
295   situations and speed up processing times, we only considered pixels within a spatial region from 135° E–15° W and 40–65° N that had an 11-12 μm BTD of less than 0.5 K, which is a fairly loose constraint for ash detection. Pixels were then flagged as 'ash' if the water vapour corrected BTD, ΔT_{ash}, was less than -0.20 K. The water vapour correction was applied following the

approach of Yu et al. (2002). After this initial ash detection threshold was applied there were generally two cases that resulted in false positives: (1) surface inversions and (2) inversions above cloud-tops. We removed these cases by setting the pixel to
300   'ash free' if:

$$-1.25 < \Delta T_{\text{ash}} < -0.20 \text{ and } T_{11} > 275 \text{ K} \tag{12}$$

or

$$-0.40 < \Delta T_{\text{ash}} < -0.20 \text{ and } T_{11} < 240 \text{ K}. \tag{13}$$

A further step to improve the 'ash flag' was to apply an 'opening' morphological 3x3 spatial filter designed to remove isolated
305   pixels unrelated to the ash cloud/plume. Finally all pixels with satellite zenith angles greater than 75 ° were ignored as the plane-parallel assumption breaks down at extreme satellite view angles.

3.5 Quality control

To ensure that only the highest quality retrievals were considered for scientific interpretation, we ran a quality control test on each pixel identified by the ash flag (Sect 3.4). The quality control checks that the retrieval converged, all state variable relative
310   uncertainties were not greater than 100 % and that the retrievals were within a physically sensible range. For the present analysis, the range of valid values considered were 0–15 μm, 0–20 and 0–35 km for r_e, τ and h_c (cloud-top height converted from p_c), respectively.

3.6 Gap filling

After ash flagging and quality control we noticed that 'gaps' in the retrieval fields were appearing where ash was originally
315   detected. Given that we have good information (quality-controlled retrievals) adjacent to these gaps, we implemented an algorithm that aims to fill the gaps in the retrieved fields. To achieve this we implemented the Qhull algorithm (Barber et al., 1996), which identifies the convex hull of a set of arbitrary points. After finding the convex hull, Delaunay triangulation is used to perform linear barycentric interpolation to fill the missing data. The gap filling algorithm was applied to all retrieved state variables and associated uncertainty fields as well as the mass loading and uncertainty computed from Eqs. 10 and 11,
320   respectively.

3.7 Parallax correction

Due to the high satellite zenith angles (∼55–75°) and high altitude of the volcanic clouds (>10 km) we also needed to correct the retrievals for parallax. We followed the method of Vicente et al. (2002) to compute the latitude/longitude parallax shift based on the ORAC retrieved height. We applied the parallax correction to all of the gap filled, quality-controlled retrievals. The
325   parallax correction resulted in pixel shifts as high as ∼ 20 km for observations at the beginning of the eruption (e.g. Fig. 3(a)). For cases where the parallax shift resulted in two solutions in the same pixel, the set of retrieved fields which corresponded to the higher height was selected. In some instances the parallax shift can leave behind gaps within the boundaries of the

volcanic cloud meaning that these pixels are being obscured by other parts of the plume. Note that the magnitude of the shift is dependent upon the retrieved height (the shift increases with increasing height for the same viewing angle). To address this,

330 we filled the parallax correction gaps by first applying a 2x2 'closing' morphological filter to the parallax-corrected ash flag and then filled the retrieval fields using the Qhull algorithm as before (Sect. 3.6).

4 Results and discussion

4.1 Raikoke source term and long-range ash transport

The June 2019 eruption from Raikoke volcano (48.292° N, 153.25° E, 551 m) is described in detail by McKee et al. (2021).

335 Here we provide an overview of the volcanic ash emissions based on AHI satellite measurements and the ORAC retrieval results. According to AHI measurements the Raikoke eruption began at around 18:00 UTC on 21 June 2019. What followed was a series of explosive eruptions characterised by sharp decreases in brightness temperatures over the volcano. Nine explosive eruptions can be clearly identified in the AHI time-series data with several smaller events more easily identified with the aid of true colour and thermal imagery.

340 Figure 3 shows a high resolution (10-minute) time-series of the ORAC cloud-top height retrievals for the Raikoke eruption sequence where we have relaxed the BTD thresholds (i.e. removed the threshold conditions in Eqs. 12 and 13) to retrieve the height in the opaque parts of the plume (Fig. 3(a)). Note that the effective radius retrievals within the opaque regions of the cloud are not reliable when using thermal-only measurements as BTDs close to zero mean that the solution space cannot be interpolated (i.e. there is no information on particle size for opaque plumes). The times-series shows maximum heights (and

345 associated uncertainty) within a 15 km radius of the volcano (Fig. 3(b)). The parallax shift is large (grey-shaded regions) for the initial Raikoke plume, demonstrating that without this correction significant errors could be introduced when comparing height and location (latitude/longitude) to other satellite datasets or dispersion model output. The first six pulses were short-lived (eruption duration from 10-40 minutes) with the seventh being the largest continuous ash emission, lasting almost 4 h. Following a pause of ∼1 h, two large explosive eruptions occurred at around 03:40 UTC and 05:30 UTC on 22 June 2019.

350 The maximum heights retrieved during the explosive phase of the eruption range from 13–14 km (asl) with numerous pulses injecting ash into the stratosphere. The major phase of the eruption had subsided by 10:00 UTC on 22 June. Based on the ORAC time-series we estimate an eruption duration of 13.8 h and a median plume-top height of 12.58 ± 2.07 km (asl).

The GOES-17 side view retrievals, with an estimated uncertainty of ± 500 m (Horváth et al., 2021a), serve as validation for heights estimated with ORAC for the initial eruption. The ORAC heights mostly agree well with the GOES-17 side

355 view heights, with some notable disagreement during the largest duration eruption and the final two pulses (Fig.3(b)). These differences are not surprising as the heights reported at these times using the GOES-17 side view method correspond to overshoots (see Supp. Mat. of Horváth et al., 2021b, for details). As the ORAC retrieval is relying on thermal infrared information to determine the plume height it is not expected to accurately capture overshoots which will likely be under-cooled (plume temperatures colder than the ambient). The ORAC heights are, however, an improvement to simply matching a brightness

360 temperature to a NWP profile as information from the 13.3 μm channel is taken into account. Further, ambiguity associated
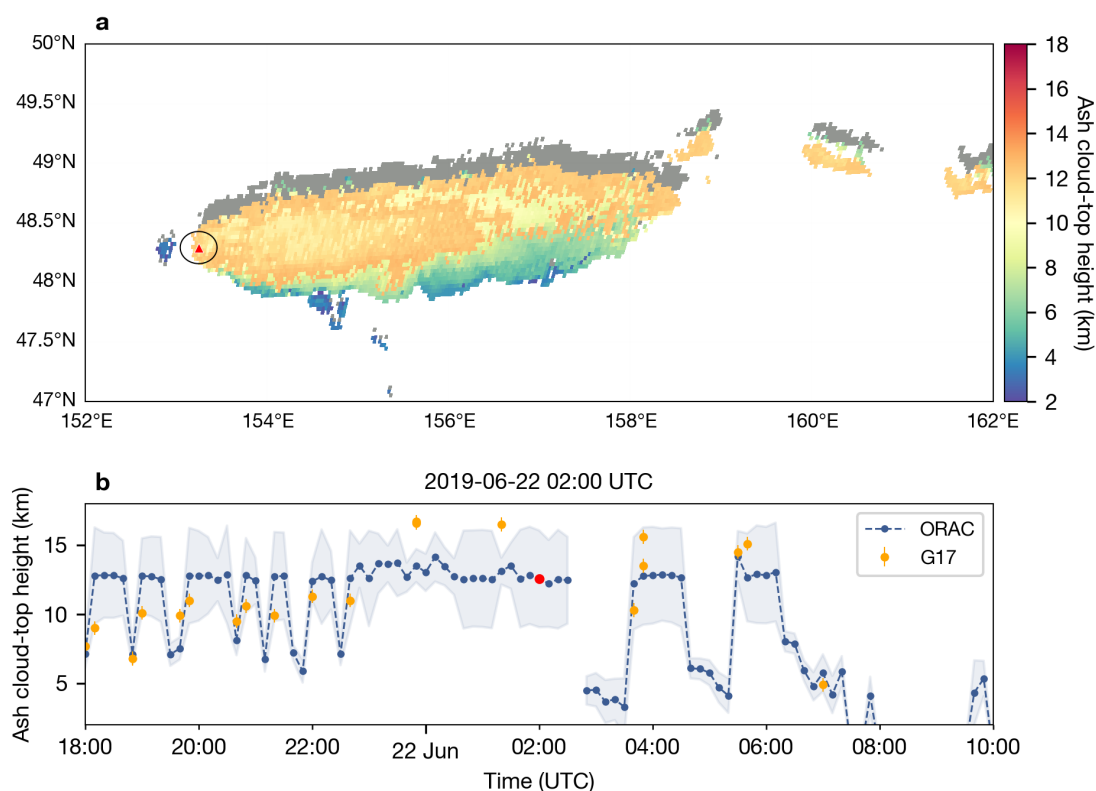
Figure 3. (a) Parallax-corrected ORAC ash cloud-top retrievals at 02:00 UTC on 22 June 2019. Grey shaded regions indicate parallax shift. Black circle indicates a 15 km radius around the volcano (red triangle). (b) High resolution (10-minute) time-series of ORAC ash cloud-top height retrievals for the Raikoke eruption. Ash cloud-top height for the ORAC retrievals (blue filled-circles) in the times-series corresponds to the maximum height within at 15 km radius of the volcano. Uncertainties associated with the ORAC heights are indicated as light blue shading around the blue filled-circles. Orange filled-circles indicate GOES-17 (G17) side-view heights taken from Horváth et al. (2021b). Orange error bars indicate ± 500 m.

with multiple height solutions (due to temperature inversions) is accounted for using optimal estimation by selecting the lowest cost from the output of the five ORAC model run configurations (described in Sect. 3.2.3).

Figure 4 shows four scenes (observation times) that illustrate the time evolution and long-range transport of the Raikoke ash cloud. The ORAC mass loading (Fig. 4(a)) and cloud-top height (Fig. 4(b)) retrievals show that ash dispersed primarily to the east with a tropospheric branch of the ash cloud separating toward the south and a stratospheric portion of the ash cloud wrapping up in a cyclone eventually resulting in ash transport toward the north. The ORAC retrievals show that the tropospheric branch of the ash cloud generally had higher mass loadings (10–$30\,\mathrm{g\,m^{-2}}$) and effective radii (4–$7\,\mu m$) whereas the stratospheric portion had comparatively lower mass loadings (1–$10\,\mathrm{g\,m^{-2}}$) and effective radii (0.5–$2.5\,\mu m$). The tropospheric

365
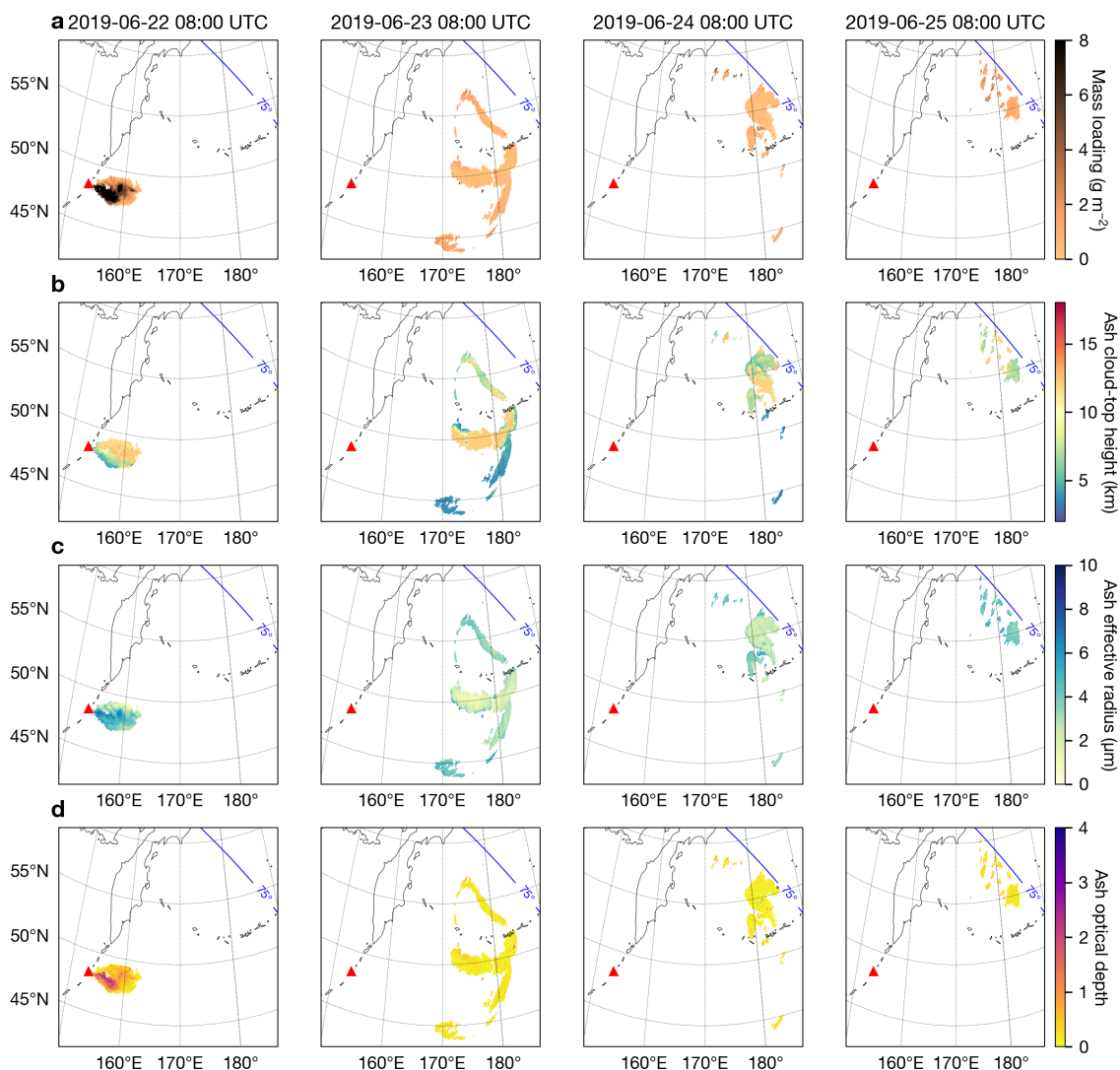
Figure 4. ORAC retrievals for (a) mass loading, (b) ash cloud-top height, (c) ash effective radius and (d) ash optical depth. Observations times annotated at the top of each column in the plot.

ash cloud maintained heights of 5–8 km whereas stratospheric ash cloud-top heights remained just above the tropopause at 11–

370   13 km. At 08:00 UTC on 23 June (Fig. 4(b) second column) there are three distinct levels in the ash cloud; a mid-tropospheric portion (3.5–4 km), a longitudinally-extended, lower-stratospheric region (12 km) and an upper-tropospheric region (6–8 km). By 08:00 UTC on 24 June the mid-tropospheric portion of the ash cloud is no longer detectable with the ash flag, while the upper-tropospheric and lower-stratospheric regions continued to disperse toward the north reaching extreme satellite view angles (where the ORAC retrievals are not possible) by 08:00 UTC on 25 June.

375   Figure 5(a) shows the time-series of total mass of very fine ash from 21 June at 18:00 UTC to 25 June at 18:00 UTC. Although our analysis period covers seven days, we found that the retrievals began to fail or gave spurious results after four days, suggesting that median optical depths of $\sim$0.1 (Fig. 5(b)) are at or close to the detection limit for the ORAC-ash retrievals applied to AHI. The peak of the total mass time series was reached $\sim$13 h after the eruption began (at 07:00 UTC on 22 June 2019) with a total mass of 0.73 $\pm$ 0.40 Tg. After reaching its maximum, the total mass decreases with an e-folding time of

380   $\sim$20 h. From 24 June onward, approximately 0.1 Tg of ash remained in the atmosphere based on the present ash detection and retrieval scheme. The ORAC estimate of the total mass of very fine ash is somewhat lower than existing estimates that also use AHI data to retrieve the total mass (e.g. 1.1 $\pm$ 0.7 Tg Muser et al., 2020). One reason for this is due to the difference in ash particle density assumed here (2300 $\pm$ 300 kgm^{-3}) and what was assumed in Muser et al. (2020) (2600 kgm^{-3}). Other differences include differing refractive index data, size distribution assumptions, the assumption of a single layer of ash vs.

385   multi-layer cloud/ash scenarios and the use of two channels to retrieve optical depth and effective radius compared to the four channels used in the present study.

The time-series of median effective radius is shown in Fig. 5(c) and reveals that larger particles ($\sim$6 μm) dominated the plume during the first $\sim$12 hours with a transition to smaller particles ($\sim$3 μm) from 12–24 h after eruption. After 60 h post-eruption there is an apparent increase in median effective radius from 3–4 μm. However, given the median satellite zenith

390   angles (Fig. 5(c) right axis) were >70° at this time, it is likely that this increase is due to a retrieval artefact rather than a real increase in particle size in the volcanic cloud.

The time-series for median cloud-top heights in the troposphere and stratosphere are shown in Fig. 5(d). We chose to plot the median cloud-top heights separately for the troposphere and stratosphere due to the distinct levels of ash that formed following the eruption. Cloud-top heights in the troposphere generally increased from 5–8 km in the first 12 h, followed by a decrease to

395   5 km after 24 h of atmospheric residence. After this period much of the ash had fallen out or was undetectable (cf. Fig. 5(a)) with the median tropospheric heights varying from 5–7 km (asl). The median stratospheric cloud-top heights remained fairly constant at 12 km throughout our analysis period with some minor variation (11-13 km). These heights are close to the chosen *a priori* stratospheric height (200 hPa) and probably reflect the fact that the measurements had little influence on the retrieved solution due to the isothermal nature of the lower-stratosphere (Fig.2).

400   ## 4.2   Total mass erupted and distal fine ash mass fraction

The total mass of very fine ash ($\leq$ 15 μm, radius) is an important piece of information for dispersion modellers attempting to forecast long-range, fine ash transport. The London VAAC parameterises the source term using an estimate of the plume-top height above vent level (H) converted to a mass eruption rate ($\dot{M}$) using the empirical fit determined by Mastin et al. (2009). The relationship has seen wide usage in the scientific literature due to its simplicity and the fact that it only requires one input

405   readily determined from satellite data. This power law relationship relates the total mass erupted (all particle sizes) to the maximum plume height (above vent level) and therefore the distal fine ash mass fraction needs to be set in order to simulate very fine ash transport and dispersion. Typical distal fine ash mass fractions used by the London VAAC range from 1-5% (Dacre et al., 2013). Based on a comparison between well-constrained values of $\dot{M}$, eruption duration and satellite retrievals,

Gouhier et al. (2019) found that the distal fine ash mass fraction varies by ∼2 orders of magnitude (0.1–6.9%) and decreases
with increasing $\dot{M}$. At the wavelengths used here the retrievals effectively measure the volume of the volcanic ash. For the
distal plume, this signal is dominated by fine ash effective radii in the range 0.1–15 µm. For the Raikoke eruption, Osborne et al.
(2022) report a total mass of 300 Tg based on the Mastin relationship ($\dot{M} = 140.8H^{1/0.241}$), assuming a plume-top height of
15 km and continuous emission from 21:00 UTC on 21 June to 03:00 UTC on 22 June (eruption duration of 6 h). It is not clear
how they arrived at the 300 Tg figure, as a constant plume height of 15 km (asl; 14.45 km above vent level) for a 6 h duration
equates to a total mass of 198 Tg when using Mastin et al.'s empirical fit. Osborne et al. (2022) caution that their total mass
estimate should only be taken as a 'representative figure' that is likely an upper-bound on the total mass due to the complexity
of the eruption source (i.e. numerous pulses, pauses and variations in plume height). The GOES-17 side-view, times-series
data show that the plume heights varied with time from 9–14 km with overshoots reaching 15–16 km. It is likely that using
a constant height of 15 km (asl) will result in a significant overestimate of the total mass, especially considering the power
law relationship between $\dot{M}$ and H. Despite this, the Osborne et al. (2022) estimate is closer to the lower range of McKee
et al. (2021) who determined total masses ranging from 287–672 Tg (average value of 439 Tg) based on more sophisticated
plume modelling constrained with plume heights ranging from 10–12 km (asl). A possible reason for this discrepancy may be
due to the fact that Osborne et al. (2022) have underestimated the eruption duration. They assume that the Raikoke eruption
started at 21:00 UTC on 21 June and ended at 03:00 UTC on 22 June, which neglects five significant eruptions at around
18:00, 18:50 and 19:40 UTC on 21 June and at around 03:40 and 05:30 UTC on 22 June (see Fig. 3(b)). McKee et al. (2021)
derive a more detailed eruption sequence of events, showing eruptive activity (recorded by infrasound, lightning and AHI
data) from around 18:00 UTC 21 June to 10:00 UTC on 22 June. However, those authors note that it is possible they have
systematically underestimated the plume-top height for the Raikoke eruption. They select the coldest pixel from T_{11} and match
it to the temperature corresponding to the highest height below the tropopause (using ERA-Interim data), despite multiple lines
of satellite-based evidence showing ash in the stratosphere at the beginning of the eruption. Therefore, the total mass estimates
from Osborne et al. (2022) and McKee et al. (2021) broadly agree but this could be because of compensating errors; Osborne
et al. (2022) overestimate the plume height and underestimate the source duration whereas McKee et al. (2021) underestimate
plume-top height.

To understand how the ORAC retrievals translate and compare to existing estimates of the total mass, we converted the time-
series of ORAC heights (Fig. 6(b)) to a time-series of $\dot{M}$ based on the Mastin relationship. We then estimated the total mass by
integrating over the $\dot{M}$ time-series. After propagating the ORAC-derived uncertainties in height through the Mastin equation
(see Appendix A), we obtain an estimate of 156 ± 88 Tg for the total mass erupted. Comparing this figure to the maximum
total mass of very fine ash derived from the ORAC mass loading retrievals, we estimate a distal fine ash mass fraction of
0.47 ± 0.37 %. Distal fine ash fractions of this magnitude are significantly lower than what is currently used by the London
VAAC (1-5%) and adds support to the Gouhier et al. (2019) finding that distal fine ash mass fractions should be set depending
on the eruption style.
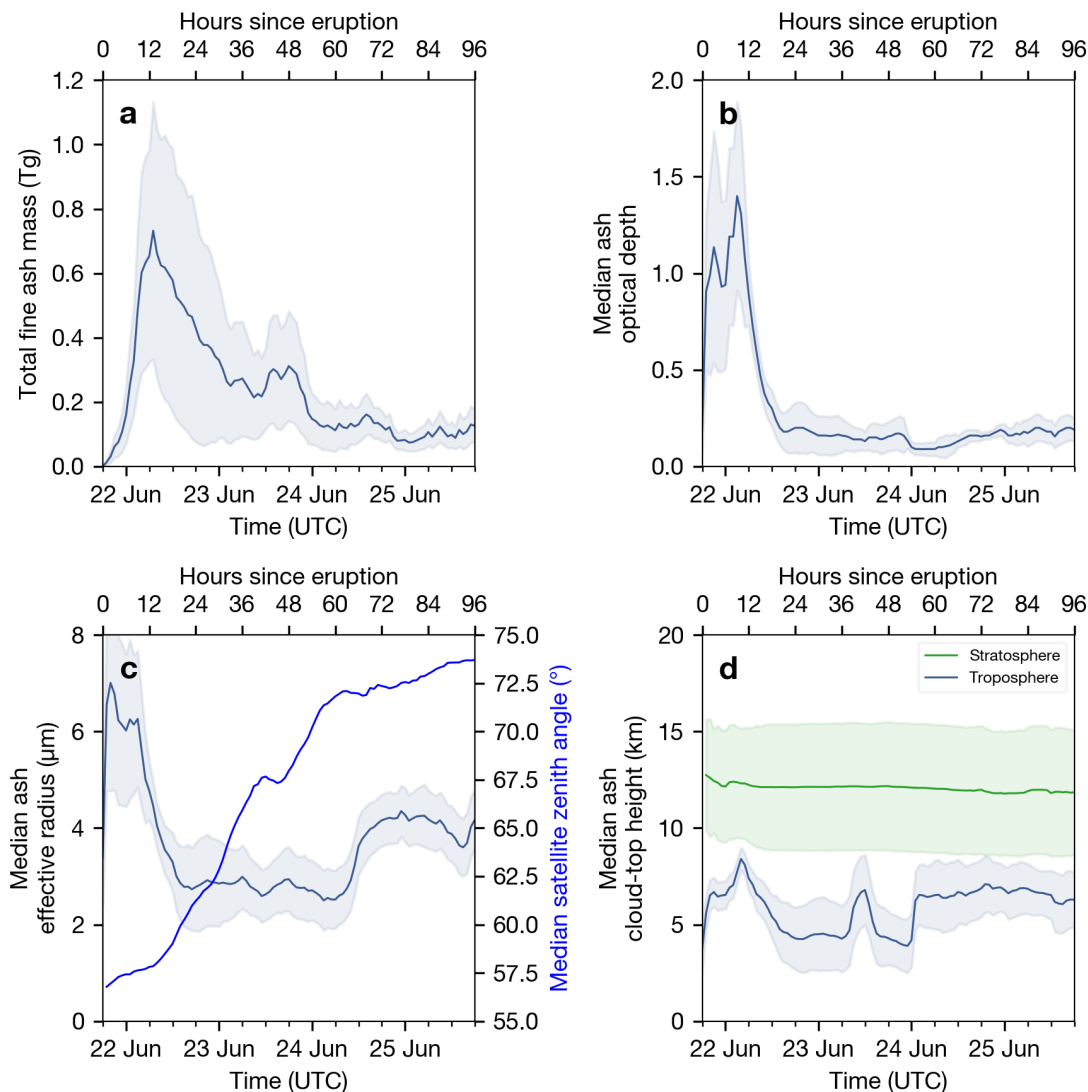
Figure 5. Time evolution of (a) total very fine ash mass, (b) median ash optical depth, (c) median ash effective radius and (d) median ash cloud-top height for the first four days of atmospheric residence following the Raikoke eruption. Shaded region in (a) represents the total mass uncertainty computed from the mass loading uncertainty fields (Eq. 11) and shaded regions in (b), (c) and (d) represent the median of the uncertainty in τ, r_e and h_c, respectively. Right axis of (c) shows the time-series of the median satellite zenith angle (bright blue line).

4.3 Ash mass loadings vs ash concentrations

Volcanic ash mass loadings represent the column mass per unit area and are distinct from ash concentrations (mass per unit volume). However, while passive imager measurements do not resolve the ash layers vertically, the mass loadings can be

445 converted to ash concentrations if a geometric thickness is assumed or measured (Sears et al., 2013). Prata and Prata (2012) demonstrated that ash concentrations could be derived from ash mass loading retrievals when combined with vertically resolved measurements from CALIOP. While only a few intersections have been identified for CALIOP for the Raikoke eruption, previous studies provide an indication of typical ash cloud geometric thicknesses. Prata et al. (2015) found that ash clouds produced by the 2008 Chaitén eruption were ∼0.3–0.7 km according to CALIOP observations. Winker et al. (2012) presented

450 CALIOP observations of the 2012 Eyjafjallajökull ash clouds and derived geometric thicknesses of 0.4–1 km. Prata et al. (2017a) studied both ash and sulphates and demonstrated that geometric thicknesses for the ash clouds produced by the 2011 Puyehue-Cordón Caulle eruption were 1.82 ± 0.55 km. Based on comparisons made with CALIPSO in the present study (Sect. 4.4), the Raikoke ash cloud geometric thicknesses were 1.04 ± 0.56 km. Figure 6 shows the median ash concentrations that would be derived if geometric thicknesses of 0.5, 1 and 2 km were assumed. The time-series demonstrates that after ∼20 h

455 the median ash concentration (for all geometric thicknesses assumed) would be fall below what ICAO regards as a 'high' ash concentration level (4 mg m^{-3}).

4.4 Cloud-top height validation

Figure 7 shows the validation results for the ORAC ash cloud-top heights. In total we found 115 collocations between the ORAC heights and the validation data derived from CALIOP and GOES-17. There is generally good agreement between the

460 ORAC heights and the validation data ($R = 0.66$). However, there is a notable negative bias (-2.22 km) for the ORAC heights. Negative biases between thermal IR height retrievals and lidar-derived heights have been observed before (Pavolonis et al., 2013; Francis et al., 2012) and is explained by the fact that the effective thermal emission height of the cloud is generally lower than the cloud-top detectable by lidar backscatter measurements. We tried to account for this by using the CALIPSO mid-layer heights (rather than layer-top heights) from the upper-most layer in the MLay product; however, the negative bias persisted.

465 The precision (standard deviation of the difference between the ORAC and validation heights) is 2.85 km, which is comparable to but somewhat higher than existing thermal IR-height retrieval schemes (cf. 1.48–1.64 km; Pavolonis et al., 2013). However, a key difference here is that we are validating height retrievals in the stratosphere and troposphere whereas previous validation studies only considered height retrievals in the troposphere.

Figure 8 shows a CALIPSO overpass where we identified the largest number of height collocations with the ORAC height

470 retrievals. This observation also serves as an important test case for height retrievals in the troposphere and stratosphere. In general, the height retrievals in the troposphere are underestimated (reflecting the negative bias seen in Fig.7). The stratospheric height retrievals show very good agreement with the CALIOP observations; however, some ORAC height retrievals returned heights in the mid-troposphere (5–6 km) when there was a stratospheric feature in the CALIOP data from 12–13 km. For these cases, the CALIOP 'Feature Optical Depth' at 532 nm for the top layer was less than 0.05 and so it is likely that the

475 stratospheric volcanic aerosol was too optically thin for the OE to determine the correct height based on the thermal radiances measured by the window channels. Additionally, if the ORAC height retrievals are underestimated, the parallax shift will also be underestimated (for the same satellite zenith angle), leading to collocation errors between AHI and CALIOP. The cloud-top height and associated uncertainty for retrievals in the stratosphere did not deviate significantly from their *a priori* values. This
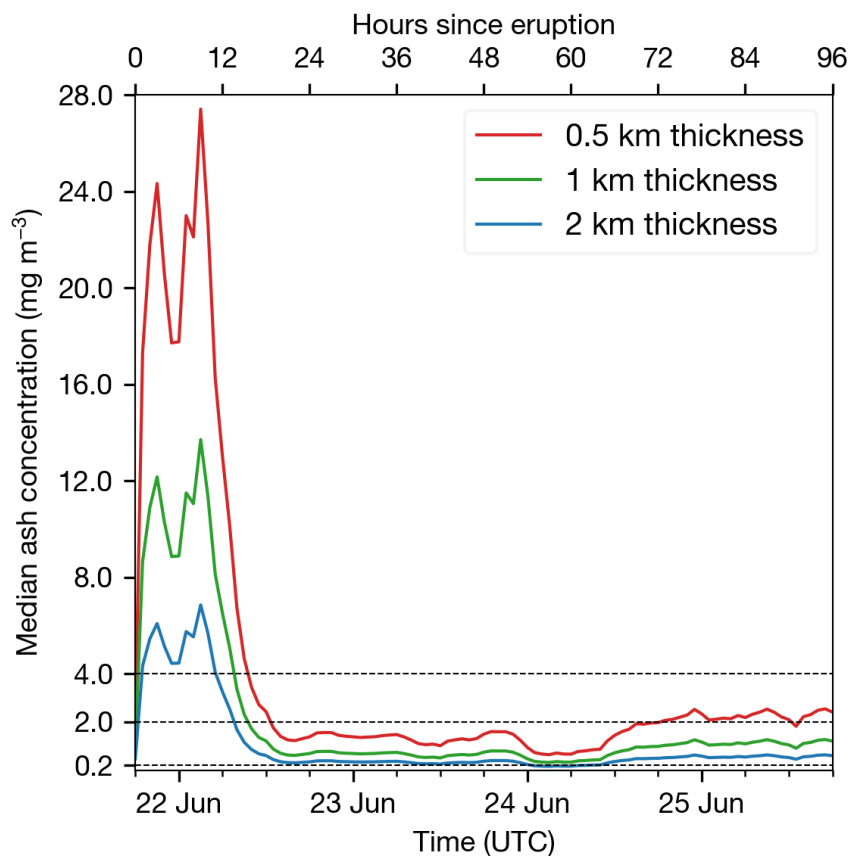
Figure 6. Time evolution of median ash concentrations produced by the Raikoke eruption assuming different geometric thicknesses. The ICAO peak ash concentration safety limits at 2 and 4 $\mathrm{mg\,m^{-3}}$ are indicated by dashed horizontal lines. The 0.2 $\mathrm{mg\,m^{-3}}$ horizonal dashed line indicates the Prata and Prata (2012) detection limit (0.2 $\mathrm{g\,m^{-2}}$) converted to an ash concentration assuming a 1 km geometric thickness.

result means that the measurements had little influence on the stratospheric height retrievals in Fig. 8(c). Although the *a priori*
480 height in the stratosphere (200 hPa) was chosen based on CALIOP observations at the beginning of the eruption, this result
highlights both the difficulty in determining height in an isothermal lower-stratosphere and the value in setting a representative
a priori in such conditions.

4.5 Importance of the 13.3 μm channel

The Raikoke case study raises several challenges for reliably retrieving ash cloud-top heights in the troposphere and strato-
485 sphere from thermal-only satellite measurements. In particular, there are two main issues: 1) the double solution due to the
inversion of temperature at the tropopause and 2) an isothermal lower stratosphere. We addressed these issues by selecting
the lowest cost from a set of FM configurations that used *a priori* pressures in the troposphere and stratosphere (described
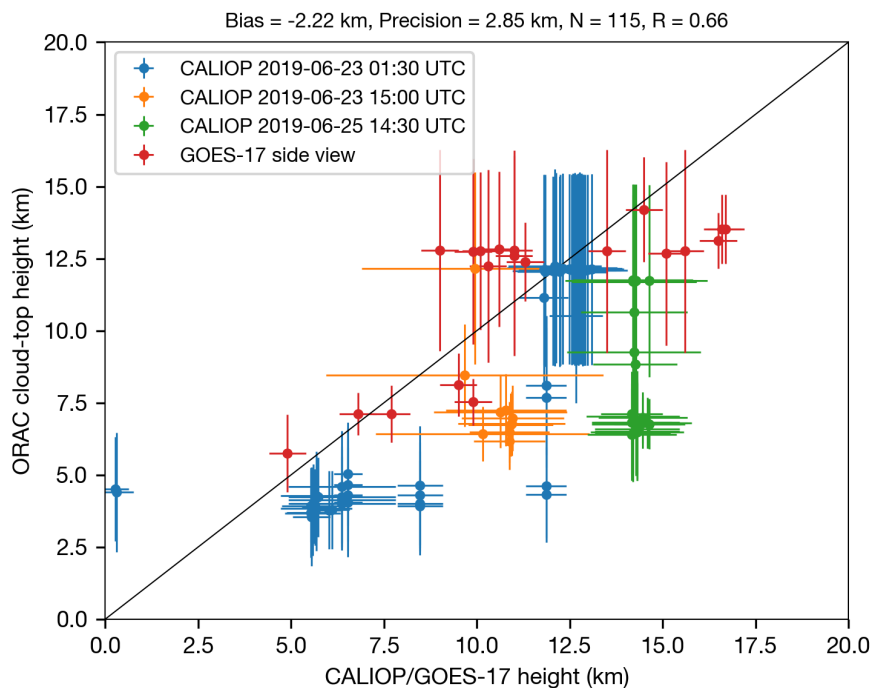
Figure 7. Validation results for the ORAC height retrievals compared to the height validation data derieved from CALIOP and GOES-17 (side view). The heights for CALIOP represent mid-layer heights (with the error bar representing the top and base heights).

in Sect. 3.2.3). To explore the robustness of this method, we ran the five FM configurations again, but removed T_{13} from the measurement vector. We found that when T_{13} was not included, the ability to select the correct retrieval solution was lost.

490   Essentially, for retrievals without the T_{13} channel, the cost for tropospheric and stratospheric height retrievals was very similar, but the stratospheric height solutions always returned the lowest cost.

Given that the information used to retrieve height comes from the thermal channels supplied to the measurement vector, the retrieval is dependent on their respective weighting functions. Figures 9(a) and (b) show the transmittance profiles and weighting functions for a clear atmosphere for each of the channels used in the measurement vector. Comparing Fig. 9(b) with

495   Fig. 9(d) shows that T_{12} is most affected by water vapour in the lower troposphere ($p > 500$ hPa) followed by T_{11} and T_{13}, with T_{10} being the least affected by water vapour. The T_{10}, T_{11} and T_{12} channel weighting functions go to zero at ∼300 hPa while the T_{13} band follows the decrease in the temperature profile (Fig. 9(c)) and remains non-zero up to ∼10 hPa. The T_{13} weighting function follows the temperature profile because it is sensitive to CO_2 absorption which is well-mixed in the atmosphere. Crucially, this variation in the weighing function in the T_{13} channel from 300 hPa to 100 hPa (and above) is what

500   allows the retrieval to distinguish between a cloud layer placed in the troposphere vs the stratosphere based on cost. Without information from the T_{13} channel, their is very little difference in TOA radiance for the simulated T_{10}, T_{11} and T_{12} channels for a cloud placed at 500 hPa (troposphere) vs 200 hPa (stratosphere) and so information from the T_{13} is key for distinguishing
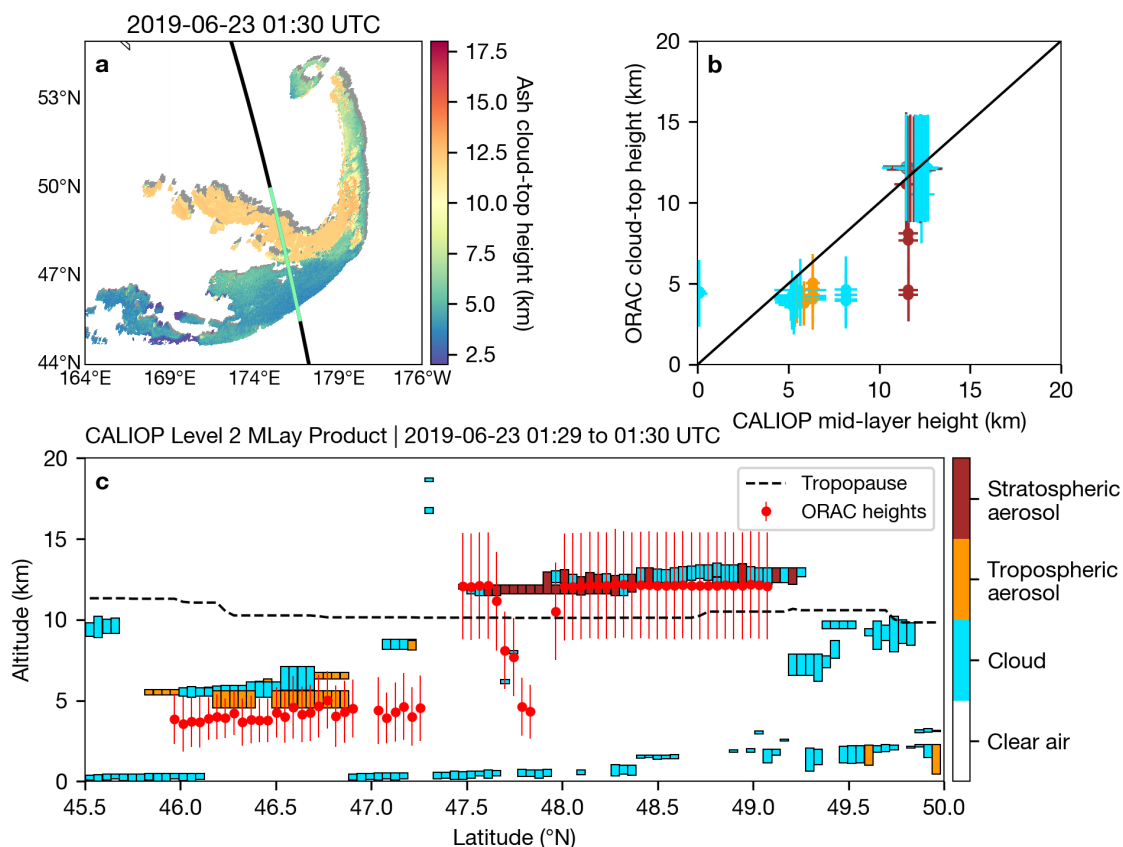
Figure 8. (a) ORAC ash cloud-top height retrievals at 1:30 UTC on 23 June 2019. Grey shaded region indicates parallax shift. (b) Correlation between ORAC ash cloud-top heights and CALIOP mid-layer heights. The colours of the data points represent the feature type identified by the CALIOP vertical feature mask (blue for cloud, orange for tropospheric aerosol and brown for stratospheric aerosol). (c) CALIOP level 2 MLay feature classification flags with collocated ORAC heights over-plotted.

between these cases. The weighting functions also show that because the lower stratosphere is isothermal, the difference in the T_{13} TOA radiance for a cloud layers placed at 200 hPa, 100 hPa and 50 hPa would be very small, meaning that for a given

505 measurement, the cost would be very similar in each case. This also explains why the retrieved heights in the stratosphere do not deviate significantly from the chosen *a priori* at 200 hPa (Fig. 8(c)).

4.6 Importance of the 10.4 μm channel

Figure 10 illustrates the importance of including the 10.4 μm channel in the measurement vector for volcanic ash retrievals using thermal-only channels. By comparing Fig. 10(a) and (b) with (c) one can see that the T_{11}-T_{12} and T_{10}-T_{11} BTDs are

510 sensitive to different effective radii sizes. The ORAC effective radius retrievals show that small particles are prevalent in the northern part of the volcanic cloud while larger particles are prevalent in the southern part. Inspection of Fig. 10(d) shows that
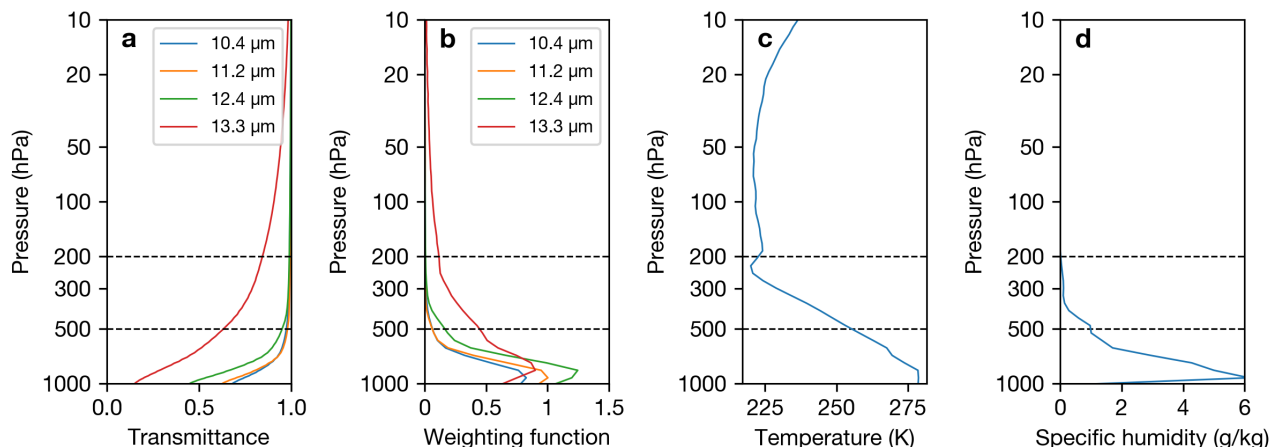
Figure 9. (a) Clear-sky transmittance profiles for the T_{10}, T_{11}, T_{12} and T_{13} AHI channels taken from the ORAC/RTTOV pre-processor output at 18:00 UTC on 22 June 2019. (b) Same as (a) but for the weighting functions. (c) ERA5 temperature profile at the same location as the clear-sky transmittance profiles. (d) Same as (c) but for specific humidity.

if we were to use a measurement vector that does not include the T_{10} channel then the solution space would be restricted to effective particle sizes larger than ∼2 µm and smaller than ∼7 µm for this particular scene. In addition, without the T_{10} channel, effective radii solutions would be found for particles in the northern part of the ash cloud but would be comparatively larger, leading to higher estimates of the total mass. On the other hand, Fig. 10(e) shows that if T_{12} was left out of the measurement vector, and T_{10} was included, then the retrieval would be sensitive to the smaller particles (for this scene ∼1–2 µm), but restricted to particle sizes smaller than ∼5 µm. In addition, a negative T_{10}-T_{11} BTD would not detect the southern part of the ash cloud (Fig. 10(b)). Therefore, by including T_{10}, T_{11} and T_{12} in the measurement vector (Fig. 10(f)) we are able to exploit the particle size information in both the T_{11}-T_{12} and T_{10}-T_{11} BTDs to optimally retrieve a wider range of effective radii sizes than existing retrieval algorithms that only exploit two channels for particle size information (e.g. Corradini et al., 2008; Prata and Prata, 2012; Francis et al., 2012; Pavolonis et al., 2013).

5 Conclusions

In this study we have presented uncertainty-bounded estimates of volcanic ash cloud-top height, optical depth, effective radius and mass loading for the June 2019 Raikoke eruption. We found the Raikoke eruption injected 0.73 ± 0.40 Tg of very fine ash into the troposphere and stratosphere. After reaching its maximum, ∼90 % of the total mass was removed from the atmosphere at an exponential decay rate of 20 h over 48 h with 0.10 Tg detectable in the atmosphere for at least four days, corresponding to median ash concentrations of ∼0.2–2 mg m^{-3} (depending on the geometric thickness assumed). The distal fine ash mass fraction was estimated to be 0.47 ± 0.37 % based on the total very fine ash mass retrieved and the ORAC cloud-top heights converted to mass eruption rates based on the Mastin relationship. Our analysis shows that the Raikoke source term is highly
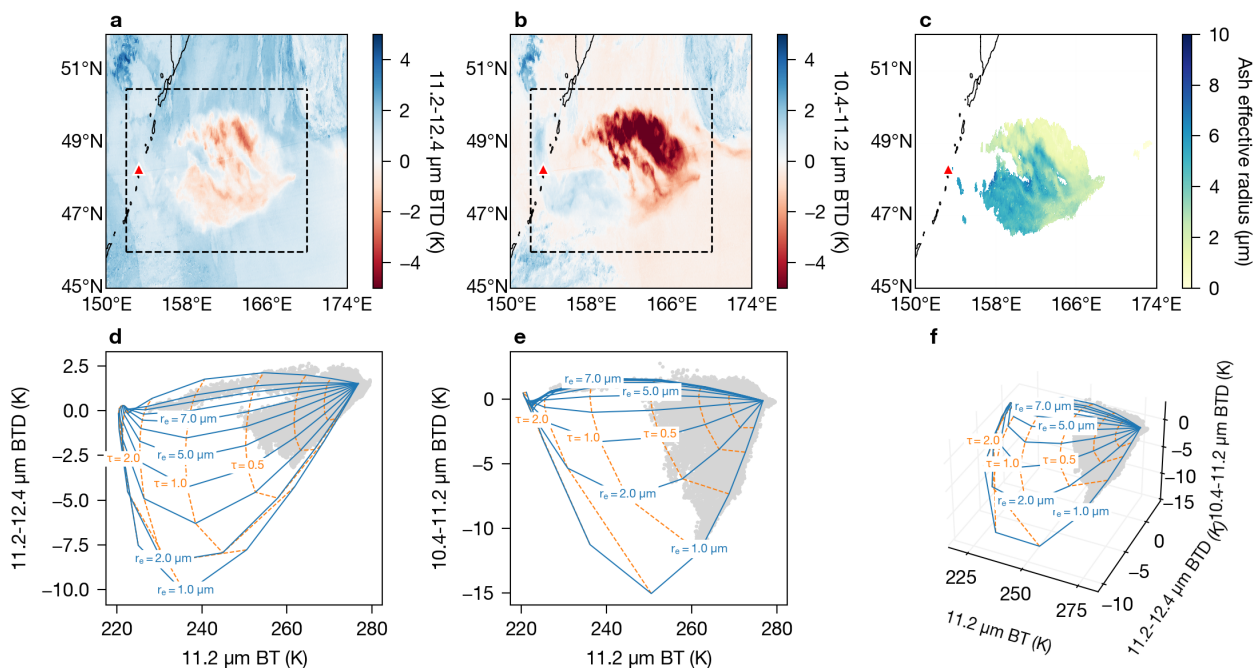
Figure 10. (a) Brightness temperature difference between T_{11} and T_{12} at 12:00 UTC on 22 June 2019. Red triangle indicates location of Raikoke. (b) Same as (a) but for a difference between T_{10} and T_{11}. (c) ORAC effective radius retrieval. (d) Two-dimensional ORAC look-up table for the complex refractive index of the 2010 Eyjafjallajökull ash (Reed et al., 2018) plotted in the T_{11} and T_{11}-T_{12} solution space. Grey data points correspond to pixels within the dashed line, bounding boxes annotated on (a). Lines of constant effective radius are plotted as blue solid lines and lines of constant optical depth (at 550 nm) are plotted as dashed orange lines. (e) same as (d) but for the T_{11} and T_{10}-T_{11} solution space. Grey data points correspond to bounding box on (b). (f) Same as (d) and (e) but for the three-dimensional, T_{11}, T_{11}-T_{12} and T_{10}-T_{11} solution space.

530 complex; meaning that eruption source parameters (i.e. injection height, duration and mass eruption rate) must be carefully considered when attempting to model this eruption. For example, due to the numerous pauses and variations in height during this eruption sequence, if a continuous eruption source with a constant maximum height is assumed then it is likely that the total mass will be overestimated. Even if the duration of the eruptions are accurately captured, underestimates or overestimates could occur if the plume height is not allowed to vary between the troposphere and stratosphere with time.

535   The ORAC algorithm represents several advances in thermal IR-based ash retrieval algorithms applied to geostationary satellite measurements. Advances include a better characterisation of measurement noise that is allowed to vary with the measured brightness temperature, the ability to distinguish between heights in the troposphere and stratosphere based on cost (with the inclusion of the T_{13} channel), the retrieval of a wider range of effective radii sizes (with the inclusion of the T_{10} channel) and accounting for underlying meteorological clouds in the FM. The ash cloud-top height retrievals showed good

540 agreement with validation data collected from CALIOP and GOES-17; however, caution must be exercised when using the

cloud-top heights retrieved in an isothermal lower-stratosphere as the retrieved solutions deviated very little from their *a priori* values. One improvement that could be made would be to use additional information, such as from dispersion model simulations, to set tightly constrained *a priori* pressure fields where ash is detected by AHI. This approach would essentially be using information from the wind fields in the stratosphere to overcome a flat cost surface due to the isothermal lower-

545 stratosphere. Other improvements include using visible channels in the measurement vector to determine optical depth and effective radius in regions of the plume that are opaque to thermal IR measurements, retrieving other multi-layer scenarios (e.g. ice above ash, ash above ash etc) and improve the ash detection flag using machine learning.

The ORAC retrievals provided here could either be used as a validation dataset for dispersion model simulations or incorporated into data assimilation schemes that require uncertainties at the grid/pixel level (e.g. Mingari et al., 2022). Incorporation of

550 these retrievals into such schemes could be used to develop quantitative now-casting/forecasting products that will aid VAACs in providing advice to airlines about quantitative ash concentrations in the future. In terms of implementing the retrieval scheme operationally, we have shown that one could use default *a priori* pressure settings in the troposphere and stratosphere and then select the run configuration with the lowest cost on a per-pixel basis to identify whether or not ash is present in the stratosphere. Height estimates could then be refined as information from independent sources becomes available (e.g. from lidar,

555 geostationary parallax and side-view heights).

Code and data availability. The ORAC code is open source and available from Github (https://github.com/ORAC-CC/orac). The ORAC 10-minute time-series of plume-top heights and 1-h retrievals (all state variables and ash flag) out to 7-days after eruption are available upon request from the corresponding author.

Appendix A: Error propagation in the Mastin equation

560 The relationship between the volumetric flow rate and the plume height has been developed over many years (Morton et al., 1956; Wilson et al., 1978; Settle, 1978; Bursik et al., 1992; Sparks et al., 1997; Mastin et al., 2009):

$$H = a\dot{V}^b, \tag{A1}$$

where H is the plume height above vent level (m), $\dot{V}$ is the volumetric flow rate (m^3/s) and a and b are free parameters determined from an empirical fit. Equation A1 can be rearranged to solve for the mass eruption rate, $\dot{M}$ (kg/s), as follows:

565 $$\dot{M} = \rho_d \left(\frac{H}{a} \right)^{1/b}, \tag{A2}$$

where $\rho_d = \dot{M}/\dot{V}$ is the 'Dense Rock Equivalent' density of tephra (all particle sizes erupted from the volcano), which is typically assumed to be 2500 kg m^{-3} (Mastin et al., 2009; Dioguardi et al., 2020). Note this density is distinct from the very fine ash particle density, ρ, which we assumed was 2300 ± 300 kgm^{-3} in the present study. If we assume all variables in

Eq. A2 are independent then we can compute the uncertainty in $\dot{M}$ from the partial derivatives as follows:

570

$$\frac{\partial \dot{M}}{\partial \rho_d} = \left(\frac{H}{a}\right)^{1/b} \tag{A3}$$

$$\frac{\partial \dot{M}}{\partial H} = \frac{1}{bH} \cdot \rho_d \left(\frac{H}{a}\right)^{1/b} \tag{A4}$$

$$\frac{\partial \dot{M}}{\partial a} = -\frac{1}{ba} \cdot \rho_d \left(\frac{H}{a}\right)^{1/b} \tag{A5}$$

575

$$\frac{\partial \dot{M}}{\partial b} = -\frac{\ln(H/a)}{b^2} \cdot \rho_d \left(\frac{H}{a}\right)^{1/b} \tag{A6}$$

The uncertainty in $\dot{M}$ is then

$$(\alpha_{\dot{M}})^2 = \left(\frac{\partial \dot{M}}{\partial \rho_d}\right)^2 (\alpha_{\rho_d})^2 + \left(\frac{\partial \dot{M}}{\partial H}\right)^2 (\alpha_H)^2 + \left(\frac{\partial \dot{M}}{\partial a}\right)^2 (\alpha_a)^2 + \left(\frac{\partial \dot{M}}{\partial b}\right)^2 (\alpha_b)^2, \tag{A7}$$

which rearranges to

580

$$\left(\frac{\alpha_{\dot{M}}}{\dot{M}}\right)^2 = \left(\frac{\alpha_{\rho_d}}{\rho_d}\right)^2 + \left(\frac{1}{b} \cdot \frac{\alpha_H}{H}\right)^2 + \left(\frac{1}{b} \cdot \frac{\alpha_a}{a}\right)^2 + \left(\frac{\ln(H/a)}{b} \cdot \frac{\alpha_b}{b}\right)^2$$

$$= \left(\frac{\alpha_{\rho_d}}{\rho_d}\right)^2 + \frac{1}{b^2}\left[\left(\frac{\alpha_H}{H}\right)^2 + \left(\frac{\alpha_a}{a}\right)^2 + \ln^2(H/a) \cdot \left(\frac{\alpha_b}{b}\right)^2\right]. \tag{A8}$$

$$\alpha_{\dot{M}} = \pm\dot{M} \cdot \sqrt{\left(\frac{\alpha_{\rho_d}}{\rho_d}\right)^2 + \frac{1}{b^2}\left[\left(\frac{\alpha_H}{H}\right)^2 + \left(\frac{\alpha_a}{a}\right)^2 + \ln^2(H/a) \cdot \left(\frac{\alpha_b}{b}\right)^2\right]}. \tag{A9}$$

From Eq. A8 we can see that the relative uncertainty in ρ_d is proportional to the relative uncertainty in $\dot{M}$ whereas an increase in the relative uncertainty in H or a will result in a factor $1/b$ increase in the relative uncertainty in $\dot{M}$. In addition, as the

585 relative uncertainty in b increases, the relative uncertainty in $\dot{M}$ will be an exponential function of H due to the $\ln(H/a)/b$ term and will thus dominate the uncertainty budget for large H (e.g. > 5.5 km; for $b = 0.241$).

To compute the total mass, M_T, and its associated uncertainty, α_{M_T}, we must integrate $\dot{M}$ with respect to time, t:

$$M_T = \int_{t_0}^{t_n} \dot{M}(t)dt. \tag{A10}$$

The above integral can be approximated as a sum of mass eruption rates multiplied by discrete time periods (i.e. the temporal

590 resolution of the satellite), Δt, so that

$$M_T \approx \sum_{i=0}^{n} \dot{M}_i \Delta t = \sum_{i=0}^{n} M_i, \tag{A11}$$

where n is the total number of observation times, $\dot{M}_i$ is the mass eruption rate at time, i, and M_i is the total mass at time, i, assuming constant $\dot{M}_i$ over Δt (note that for AHI, $\Delta t = 600$ s). The uncertainty in the total mass can therefore be written as

$$(\alpha_{M_T})^2 = (\alpha_{M_1})^2 + (\alpha_{M_2})^2 + \cdots + (\alpha_{M_n})^2 \qquad (A12)$$

595
$$\alpha_{M_T} = \pm\Delta t\sqrt{(\alpha_{\dot{M}_1})^2 + (\alpha_{\dot{M}_2})^2 + \cdots + (\alpha_{\dot{M}_n})^2}, \qquad (A13)$$

where we assume errors across each time step are uncorrelated. To evaluate $\dot{M}$ and $\alpha_{\dot{M}}$ at all observation times using Eqs. A2 and A9, we use the ORAC height time-series shown in Fig. 3. Note that H is determined from the ORAC-retrieved height, h_c, via $H = h_c - h_v$, where h_v is the vent height of the Raikoke volcano (0.551 km above sea level). For ρ_d, a and b, we use the values provided in Mastin et al. (2009), which are 2500 kg m^{-3}, 2.00 and 0.241, respectively. Uncertainty in H is taken from
600 the ORAC retrievals. Uncertainty in ρ_d is not provided in Mastin et al. (2009) and so we conservatively assumed a relative uncertainty on ρ_d of 50%. This value may seem high, but when propagated through Eqs. A9 and A13 the difference between a relative uncertainty of 10% and 50% converts to a different in absolute uncertainty in the total mass of $\sim$1 Tg. Uncertainty associated with the a and b parameters is related to the sample size, eruption type and errors in plume height and volumetric flow rate taken from the cases used in the empirical fit. Based on the range of values reported and discussed in the literature
605 (e.g. Bursik et al., 1992; Sparks et al., 1997; Mastin et al., 2009) and noting the theoretical finding that $\dot{M}$ is related to H to the fourth power (i.e. $b = 0.25$; Morton et al., 1956), we assumed relative uncertainties on a and b of 90% and 20%, respectively.

Finally, the distal fine ash mass fraction, m_f, is computed as

$$m_f = \frac{m_T}{M_T}, \qquad (A14)$$

where m_T is the maximum total fine ash mass retrieved determined from ORAC. The associated uncertainty in m_f is

610
$$\alpha_{m_f} = \pm m_f \cdot \sqrt{\left(\frac{\alpha_{m_T}}{m_T}\right)^2 + \left(\frac{\alpha_{M_T}}{M_T}\right)^2}, \qquad (A15)$$

where α_{m_T} is the uncertainty associated with the maximum total mass of very fine ash determined from ORAC.

Author contributions. ATP, RGG and IAT developed the ideas for the manuscript. ATP led the writing of the manuscript, ran the satellite retrievals and conducted the data analysis. RGG, ACP, SRP, ATP and CP are developers of the ORAC software and made improvements to the code for the purposes of this study. All authors contributed to data interpretation and writing of the manuscript.

615 *Competing interests.* The authors declare no competing interests.

Acknowledgements. RGG and IAT were supported by the NERC Centre for Observation and Modelling of Earthquakes, Volcanoes, and Tectonics (COMET). This study was funded as part of NERC's support of the National Centre for Earth Observation, contract number

PR140015. ATP and RGG acknowledge funding from the NERC R4AsH project NE/S003843/1. IAT and RGG acknowledge funding from the NERC V-Plus project NE/S004025/1.

620 **References**

Barber, C. B., Dobkin, D. P., and Huhdanpaa, H.: The quickhull algorithm for convex hulls, ACM Transactions on Mathematical Software,
22, 469–483, https://doi.org/10.1145/235815.235821, 1996.

Bessho, K., Date, K., Hayashi, M., Ikeda, A., Imai, T., Inoue, H., Kumagai, Y., Miyakawa, T., Murata, H., Ohno, T., Okuyama, A., Oyama,
R., Sasaki, Y., Shimazu, Y., Shimoji, K., Sumida, Y., Suzuki, M., Taniguchi, H., Tsuchiyama, H., Uesawa, D., Yokota, H., and Yoshida,
625 R.: An Introduction to Himawari-8/9–Japan's New-Generation Geostationary Meteorological Satellites, Journal of the Meteorological
Society of Japan. Ser. II, 94, 151–183, https://doi.org/10.2151/jmsj.2016-009, 2016.

Bursik, M. I., Sparks, R. S. J., Gilbert, J. S., and Carey, S. N.: Sedimentation of tephra by volcanic plumes: I. Theory and its comparison with
a study of the Fogo A plinian deposit, Sao Miguel (Azores), Bulletin of Volcanology, 54, 329–344, https://doi.org/10.1007/BF00301486,
1992.

630 Cooper, S. J., L'Ecuyer, T. S., Gabriel, P., Baran, A. J., and Stephens, G. L.: Objective Assessment of the Information Content of Visible
and Infrared Radiance Measurements for Cloud Microphysical Property Retrievals over the Global Oceans. Part II: Ice Clouds, Journal of
Applied Meteorology and Climatology, 45, 42–62, https://doi.org/10.1175/JAM2327.1, 2006.

Corradini, S., Spinetti, C., Carboni, E., Tirelli, C., Buongiorno, M., Pugnaghi, S., and Gangale, G.: Mt. Etna tropospheric ash retrieval and
sensitivity analysis using moderate resolution imaging spectroradiometer measurements, Journal of Applied Remote Sensing, 2, 023 550,
635 https://doi.org/10.1117/1.3046674, 2008.

Corradini, S., Montopoli, M., Guerrieri, L., Ricci, M., Scollo, S., Merucci, L., Marzano, F., Pugnaghi, S., Prestifilippo, M., Ventress, L.,
Grainger, R., Carboni, E., Vulpiani, G., and Coltelli, M.: A Multi-Sensor Approach for Volcanic Ash Cloud Retrieval and Eruption
Characterization: The 23 November 2013 Etna Lava Fountain, Remote Sensing, 8, 58, https://doi.org/10.3390/rs8010058, 2016.

Dacre, H. F., Grant, A. L. M., and Johnson, B. T.: Aircraft observations and model simulations of concentration and particle size distribution in
640 the Eyjafjallajökull volcanic ash cloud, Atmospheric Chemistry and Physics, 13, 1277–1291, https://doi.org/10.5194/acp-13-1277-2013,
2013.

de Leeuw, J., Schmidt, A., Witham, C. S., Theys, N., Taylor, I. A., Grainger, R. G., Pope, R. J., Haywood, J., Osborne, M., and Kristiansen,
N. I.: The 2019 Raikoke volcanic eruption – Part 1: Dispersion model simulations and satellite retrievals of volcanic sulfur dioxide,
Atmospheric Chemistry and Physics, 21, 10 851–10 879, https://doi.org/10.5194/acp-21-10851-2021, 2021.

645 Dioguardi, F., Beckett, F., Dürig, T., and Stevenson, J. A.: The Impact of Eruption Source Parameter Uncertainties on Ash Dispersion Fore-
casts During Explosive Volcanic Eruptions, Journal of Geophysical Research: Atmospheres, 125, https://doi.org/10.1029/2020JD032717,
2020.

Folch, A., Mingari, L., Gutierrez, N., Hanzich, M., Macedonio, G., and Costa, A.: FALL3D-8.0: a computational model for atmospheric
transport and deposition of particles, aerosols and radionuclides – Part 1: Model physics and numerics, Geoscientific Model Development,
650 13, 1431–1458, https://doi.org/10.5194/gmd-13-1431-2020, 2020.

Folch, A., Mingari, L., and Prata, A. T.: Ensemble-Based Forecast of Volcanic Clouds Using FALL3D-8.1, Frontiers in Earth Science, 9,
741 841, https://doi.org/10.3389/feart.2021.741841, 2022.

Francis, P. N., Cooke, M. C., and Saunders, R. W.: Retrieval of physical properties of volcanic ash using Meteosat: A case study from the
2010 Eyjafjallajökull eruption, Journal of Geophysical Research: Atmospheres, 117, https://doi.org/10.1029/2011JD016788, 2012.

655 Gouhier, M., Eychenne, J., Azzaoui, N., Guillin, A., Deslandes, M., Poret, M., Costa, A., and Husson, P.: Low efficiency of large volcanic
eruptions in transporting very fine ash into the atmosphere, Scientific Reports, 9, https://doi.org/10.1038/s41598-019-38595-7, 2019.

Grainger, R. G., Peters, D. M., Thomas, G. E., Smith, A. J. A., Siddans, R., Carboni, E., and Dudhia, A.: Measuring volcanic plume and ash properties from space, Geological Society, London, Special Publications, 380, 293–320, https://doi.org/10.1144/SP380.7, 2013.

Gu, Y., Rose, W. I., and Bluth, G. J. S.: Retrieval of mass and sizes of particles in sandstorms using two MODIS IR bands: A case study of April 7, 2001 sandstorm in China, Geophysical Research Letters, 30, https://doi.org/10.1029/2003GL017405, 2003.

Harvey, N. J., Dacre, H. F., Webster, H. N., Taylor, I. A., Khanal, S., Grainger, R. G., and Cooke, M. C.: The Impact of Ensemble Meteorology on Inverse Modeling Estimates of Volcano Emissions and Ash Dispersion Forecasts: Grímsvötn 2011, Atmosphere, 11, 1022, https://doi.org/10.3390/atmos11101022, 2020.

Harvey, N. J., Dacre, H. F., Saint, C., Prata, A., Webster, H. N., and Grainger, R. G.: Quantifying the impact of meteorological uncertainty on emission estimates and volcanic ash forecasts of the Raikoke 2019 eruption, preprint, Dynamics/Atmospheric Modelling/Troposphere/Physics (physical properties and processes), https://doi.org/10.5194/acp-2021-973, 2022.

Heidinger, A. K., Pavolonis, M. J., Holz, R. E., Baum, B. A., and Berthier, S.: Using CALIPSO to explore the sensitivity to cirrus height in the infrared observations from NPOESS/VIIRS and GOES-R/ABI, Journal of Geophysical Research, 115, D00H20, https://doi.org/10.1029/2009JD012152, 2010.

Hersbach, H., Bell, B., Berrisford, P., Hirahara, S., Horányi, A., Muñoz-Sabater, J., Nicolas, J., Peubey, C., Radu, R., Schepers, D., Simmons, A., Soci, C., Abdalla, S., Abellan, X., Balsamo, G., Bechtold, P., Biavati, G., Bidlot, J., Bonavita, M., Chiara, G., Dahlgren, P., Dee, D., Diamantakis, M., Dragani, R., Flemming, J., Forbes, R., Fuentes, M., Geer, A., Haimberger, L., Healy, S., Hogan, R. J., Hólm, E., Janisková, M., Keeley, S., Laloyaux, P., Lopez, P., Lupu, C., Radnoti, G., Rosnay, P., Rozum, I., Vamborg, F., Villaume, S., and Thépaut, J.: The ERA5 global reanalysis, Quarterly Journal of the Royal Meteorological Society, 146, 1999–2049, https://doi.org/10.1002/qj.3803, 2020.

Horváth, , Carr, J. L., Girina, O. A., Wu, D. L., Bril, A. A., Mazurov, A. A., Melnikov, D. V., Hoshyaripour, G. A., and Buehler, S. A.: Geometric estimation of volcanic eruption column height from GOES-R near-limb imagery – Part 1: Methodology, Atmospheric Chemistry and Physics, 21, 12 189–12 206, https://doi.org/10.5194/acp-21-12189-2021, 2021a.

Horváth, , Girina, O. A., Carr, J. L., Wu, D. L., Bril, A. A., Mazurov, A. A., Melnikov, D. V., Hoshyaripour, G. A., and Buehler, S. A.: Geometric estimation of volcanic eruption column height from GOES-R near-limb imagery – Part 2: Case studies, Atmospheric Chemistry and Physics, 21, 12 207–12 226, https://doi.org/10.5194/acp-21-12207-2021, 2021b.

Hyman, D. M. and Pavolonis, M. J.: Probabilistic retrieval of volcanic SO2 layer height and cumulative mass loading using the Cross-track Infrared Sounder (CrIS), https://doi.org/10.5194/amt-2020-41, 2020.

ICAO: Roadmap for International Airways Volcano Watch (IAVW) in Support of International Air Navigation (last access: 29 November 2021), https://www.icao.int/airnavigation/METP/MOGVARReferenceDocuments/IAVW20Roadmap.pdf, 2019.

Inoue, T.: On the Temperature and Effective Emissivity Determination of Semi-Transparent Cirrus Clouds by Bi-Spectral Measurements in the 10 μm Window Region, Journal of the Meteorological Society of Japan. Ser. II, 63, 88–99, https://doi.org/10.2151/jmsj1965.63.1_88, 1985.

Iwabuchi, H. and Hayasaka, T.: Effects of Cloud Horizontal Inhomogeneity on the Optical Thickness Retrieved from Moderate-Resolution Satellite Data, Journal of the Atmospheric Sciences, 59, 2227–2242, https://doi.org/https://doi.org/10.1175/1520-0469(2002)059<2227:EOCHIO>2.0.CO;2, 2002.

Key, J. R.: Retrieval of cloud optical depth and particle effective radius at high latitudes using visible and thermal satellite data, p. 318, Paris, France, https://doi.org/10.1117/12.228928, 1995.

Kylling, A., Kahnert, M., Lindqvist, H., and Nousiainen, T.: Volcanic ash infrared signature: porous non-spherical ash particle shapes compared to homogeneous spherical ash particles, Atmospheric Measurement Techniques, 7, 919–929, https://doi.org/10.5194/amt-7-919-2014, 2014.

Kylling, A., Kristiansen, N., Stohl, A., Buras-Schnell, R., Emde, C., and Gasteiger, J.: A model sensitivity study of the impact of clouds on satellite detection and retrieval of volcanic ash, Atmospheric Measurement Techniques, 8, 1935–1949, https://doi.org/10.5194/amt-8-1935-2015, 2015.

Levenberg, K.: A method for the solution of certain non-linear problems in least squares, Quarterly of Applied Mathematics, 2, 164–168, https://doi.org/10.1090/qam/10666, 1944.

Lindsey, D., Schmit, T. J., MacKenzie, W. M., Jewitt, C. P., Gunshor, M. M., and Grasso, L.: 10.35 μm: atmospheric window on the GOES-R Advanced Baseline Imager with less moisture attenuation, Journal of Applied Remote Sensing, 6, 1, https://doi.org/10.1117/1.JRS.6.063598, 2012.

Lu, S., Lin, H. X., Heemink, A., Segers, A., and Fu, G.: Estimation of volcanic ash emissions through assimilating satellite data and ground-based observations, Journal of Geophysical Research: Atmospheres, 121, 10,971–10,994, https://doi.org/10.1002/2016JD025131, 2016.

Mackie, S., Millington, S., and Watson, I. M.: How assumed composition affects the interpretation of satellite observations of volcanic ash: How assumed composition affects interpretation of ash observations, Meteorological Applications, 21, 20–29, https://doi.org/10.1002/met.1445, 2014.

Marquardt, D. W.: An Algorithm for Least-Squares Estimation of Nonlinear Parameters, Journal of the Society for Industrial and Applied Mathematics, 11, 431–441, https://doi.org/10.1137/0111030, 1963.

Mastin, L., Guffanti, M., Servranckx, R., Webley, P., Barsotti, S., Dean, K., Durant, A., Ewert, J., Neri, A., Rose, W., Schneider, D., Siebert, L., Stunder, B., Swanson, G., Tupper, A., Volentik, A., and Waythomas, C.: A multidisciplinary effort to assign realistic source parameters to models of volcanic ash-cloud transport and dispersion during eruptions, Journal of Volcanology and Geothermal Research, 186, 10–21, https://doi.org/10.1016/j.jvolgeores.2009.01.008, 2009.

McGarragh, G. R., Poulsen, C. A., Thomas, G. E., Povey, A. C., Sus, O., Stapelberg, S., Schlundt, C., Proud, S., Christensen, M. W., Stengel, M., Hollmann, R., and Grainger, R. G.: The Community Cloud retrieval for CLimate (CC4CL) – Part 2: The optimal estimation approach, Atmospheric Measurement Techniques, 11, 3397–3431, https://doi.org/10.5194/amt-11-3397-2018, 2018.

McKee, K., Smith, C. M., Reath, K., Snee, E., Maher, S., Matoza, R. S., Carn, S., Mastin, L., Anderson, K., Damby, D., Roman, D. C., Degterev, A., Rybin, A., Chibisova, M., Assink, J. D., de Negri Leiva, R., and Perttu, A.: Evaluating the state-of-the-art in remote volcanic eruption characterization Part I: Raikoke volcano, Kuril Islands, Journal of Volcanology and Geothermal Research, 419, 107 354, https://doi.org/10.1016/j.jvolgeores.2021.107354, 2021.

Mingari, L., Folch, A., Prata, A. T., Pardini, F., Macedonio, G., and Costa, A.: Data assimilation of volcanic aerosol observations using FALL3D+PDAF, Atmospheric Chemistry and Physics, 22, 1773–1792, https://doi.org/10.5194/acp-22-1773-2022, 2022.

Morton, B. R., Taylor, G T, and Turner, J S: Turbulent gravitational convection from maintained and instantaneous sources, Proceedings of the Royal Society of London. Series A. Mathematical and Physical Sciences, 234, 1–23, https://doi.org/10.1098/rspa.1956.0011, 1956.

Muser, L. O., Hoshyaripour, G. A., Bruckert, J., Horváth, , Malinina, E., Wallis, S., Prata, F. J., Rozanov, A., von Savigny, C., Vogel, H., and Vogel, B.: Particle aging and aerosol–radiation interaction affect volcanic plume dispersion: evidence from the Raikoke 2019 eruption, Atmospheric Chemistry and Physics, 20, 15 015–15 036, https://doi.org/10.5194/acp-20-15015-2020, 2020.

Osborne, M. J., de Leeuw, J., Witham, C., Schmidt, A., Beckett, F., Kristiansen, N., Buxmann, J., Saint, C., Welton, E. J., Fochesatto, J., Gomes, A. R., Bundke, U., Petzold, A., Marenco, F., and Haywood, J.: The 2019 Raikoke volcanic eruption – Part 2: Particle-phase

dispersion and concurrent wildfire smoke emissions, Atmospheric Chemistry and Physics, 22, 2975–2997, https://doi.org/10.5194/acp-22-2975-2022, 2022.

Pardini, F., Corradini, S., Costa, A., Esposti Ongaro, T., Merucci, L., Neri, A., Stelitano, D., and de' Michieli Vitturi, M.: Ensemble-Based
735   Data Assimilation of Volcanic Ash Clouds from Satellite Observations: Application to the 24 December 2018 Mt. Etna Explosive Eruption, Atmosphere, 11, 359, https://doi.org/10.3390/atmos11040359, 2020.

Parol, F., Buriez, J. C., Brogniez, G., and Fouquart, Y.: Information Content of AVHRR Channels 4 and 5 with Respect to the Effective Radius of Cirrus Cloud Particles, Journal of Applied Meteorology, 30, 973–984, https://doi.org/10.1175/1520-0450-30.7.973, 1991.

Pavolonis, M. and Sieglaff, J.: GOES-R Advanced Baseline Imager (ABI) Algorithm Theoretical Basis Document For Volcanic Ash (Detec-
740   tion and Height), p. 71, 2012.

Pavolonis, M. J., Heidinger, A. K., and Sieglaff, J.: Automated retrievals of volcanic ash and dust cloud properties from upwelling infrared measurements: Retrieval of ash/dust cloud properties, Journal of Geophysical Research: Atmospheres, 118, 1436–1458, https://doi.org/10.1002/jgrd.50173, 2013.

Pavolonis, M. J., Sieglaff, J., and Cintineo, J.: Spectrally Enhanced Cloud Objects-A generalized framework for automated detection of
745   volcanic ash and dust clouds using passive satellite measurements: 2. Cloud object analysis and global application, Journal of Geophysical Research: Atmospheres, 120, 7842–7870, https://doi.org/10.1002/2014JD022969, 2015a.

Pavolonis, M. J., Sieglaff, J., and Cintineo, J.: Spectrally Enhanced Cloud Objects-A generalized framework for automated detection of volcanic ash and dust clouds using passive satellite measurements: 1. Multispectral analysis, Journal of Geophysical Research: Atmospheres, 120, 7813–7841, https://doi.org/10.1002/2014JD022968, 2015b.

750 Pavolonis, M. J., Sieglaff, J. M., and Cintineo, J. L.: Remote Sensing of Volcanic Ash with the GOES-R Series, in: The GOES-R Series, pp. 103–124, Elsevier, https://doi.org/10.1016/B978-0-12-814327-8.00010-X, 2020.

Pouget, S., Bursik, M., Webley, P., Dehn, J., and Pavolonis, M.: Estimation of eruption source parameters from umbrella cloud or downwind plume growth rate, Journal of Volcanology and Geothermal Research, 258, 100–112, https://doi.org/10.1016/j.jvolgeores.2013.04.002, 2013.

755 Poulsen, C. A., Siddans, R., Thomas, G. E., Sayer, A. M., Grainger, R. G., Campmany, E., Dean, S. M., Arnold, C., and Watts, P. D.: Cloud retrievals from satellite data using optimal estimation: evaluation and application to ATSR, Atmospheric Measurement Techniques, 5, 1889–1910, https://doi.org/10.5194/amt-5-1889-2012, 2012.

Prabhakara, C., Fraser, R. S., Dalu, G., Wu, M.-L. C., Curran, R. J., and Styles, T.: Thin Cirrus Clouds: Seasonal Distribution over Oceans Deduced from Nimbus-4 IRIS, Journal of Applied Meteorology, 27, 379–399, https://doi.org/10.1175/1520-
760   0450(1988)027<0379:TCCSDO>2.0.CO;2, 1988.

Prata, A. J.: Infrared radiative transfer calculations for volcanic ash clouds, Geophysical Research Letters, 16, 1293–1296, https://doi.org/10.1029/GL016i011p01293, 1989a.

Prata, A. J.: Observations of volcanic ash clouds in the 10-12 μm window using AVHRR/2 data, International Journal of Remote Sensing, 10, 751–761, https://doi.org/10.1080/01431168908903916, 1989b.

765 Prata, A. J. and Grant, I. F.: Retrieval of microphysical and morphological properties of volcanic ash plumes from satellite data: Application to Mt Ruapehu, New Zealand, Quarterly Journal of the Royal Meteorological Society, 127, 2153–2179, https://doi.org/10.1002/qj.49712757615, 2001.

Prata, A. J. and Prata, A. T.: Eyjafjallajökull volcanic ash concentrations determined using Spin Enhanced Visible and Infrared Imager measurements, Journal of Geophysical Research: Atmospheres, 117, https://doi.org/10.1029/2011JD016800, 2012.

770   Prata, A. T., Siems, S. T., and Manton, M. J.: Quantification of volcanic cloud top heights and thicknesses using A-train observations for the
       2008 Chaitén eruption, Journal of Geophysical Research: Atmospheres, 120, 2928–2950, https://doi.org/10.1002/2014JD022399, 2015.

Prata, A. T., Young, S. A., Siems, S. T., and Manton, M. J.: Lidar ratios of stratospheric volcanic ash and sulfate aerosols retrieved from
       CALIOP measurements, Atmospheric Chemistry and Physics, 17, 8599–8618, https://doi.org/10.5194/acp-17-8599-2017, 2017a.

Prata, A. T., Folch, A., Prata, A. J., Biondi, R., Brenot, H., Cimarelli, C., Corradini, S., Lapierre, J., and Costa, A.: Anak Krakatau triggers
775   volcanic freezer in the upper troposphere, Scientific Reports, 10, https://doi.org/10.1038/s41598-020-60465-w, 2020.

Prata, A. T., Mingari, L., Folch, A., Macedonio, G., and Costa, A.: FALL3D-8.0: a computational model for atmospheric transport
       and deposition of particles, aerosols and radionuclides – Part 2: Model validation, Geoscientific Model Development, 14, 409–436,
       https://doi.org/10.5194/gmd-14-409-2021, 2021.

Prata, F., Woodhouse, M., Huppert, H. E., Prata, A., Thordarson, T., and Carn, S.: Atmospheric processes affecting the separation of volcanic
780   ash and SO_2 in volcanic eruptions: inferences from the May 2011 Grímsvötn eruption, Atmospheric Chemistry and Physics, 17, 10 709–
       10 732, https://doi.org/10.5194/acp-17-10709-2017, 2017b.

Prata, G. S., Ventress, L. J., Carboni, E., Mather, T. A., Grainger, R. G., and Pyle, D. M.: A New Parameterization of Volcanic Ash
       Complex Refractive Index Based on NBO/T and SiO_2 Content, Journal of Geophysical Research: Atmospheres, 124, 1779–1797,
       https://doi.org/10.1029/2018JD028679, 2019.

785   Reed, B. E., Peters, D. M., McPheat, R., and Grainger, R. G.: The Complex Refractive Index of Volcanic Ash Aerosol Retrieved From Spectral
       Mass Extinction, Journal of Geophysical Research: Atmospheres, 123, 1339–1350, https://doi.org/10.1002/2017JD027362, 2018.

Rodgers, C. D.: Retrieval of atmospheric temperature and composition from remote measurements of thermal radiation, Reviews of Geo-
       physics, 14, 609, https://doi.org/10.1029/RG014i004p00609, 1976.

Rodgers, C. D.: Inverse methods for atmospheric sounding : theory and practice, World Scientific, Singapore, 2000.

790   Saunders, R., Hocking, J., Turner, E., Rayer, P., Rundle, D., Brunel, P., Vidot, J., Roquet, P., Matricardi, M., Geer, A., Bormann, N., and Lupu,
       C.: An update on the RTTOV fast radiative transfer model (currently at version 12), Geoscientific Model Development, 11, 2717–2737,
       https://doi.org/10.5194/gmd-11-2717-2018, 2018.

Schneider, D. J., Rose, W. I., Coke, L. R., Bluth, G. J. S., Sprod, I. E., and Krueger, A. J.: Early evolution of a stratospheric
       volcanic eruption cloud as observed with TOMS and AVHRR, Journal of Geophysical Research: Atmospheres, 104, 4037–4050,
795   https://doi.org/10.1029/1998JD200073, 1999.

Sears, T. M., Thomas, G. E., Carboni, E., A. Smith, A. J., and Grainger, R. G.: SO_2 as a possible proxy for volcanic ash in aviation hazard
       avoidance, Journal of Geophysical Research: Atmospheres, 118, 5698–5709, https://doi.org/10.1002/jgrd.50505, 2013.

Settle, M.: Volcanic eruption clouds and the thermal power output of explosive eruptions, Journal of Volcanology and Geothermal Research,
       3, 309–324, https://doi.org/10.1016/0377-0273(78)90041-0, 1978.

800   Soda, R.: Infrared Absorption Spectra of Quartz and Some other Silica Modification, Bulletin of the Chemical Society of Japan, 34, 1491–
       1495, https://doi.org/10.1246/bcsj.34.1491, 1961.

Sparks, R. S. J., Bursik, M. I., Carey, S. N., Gilbert, J., Glaze, L. S., Sigurdsson, H., and Woods, A.: Volcanic Plumes, Wiley, 1997.

Stamnes, K., Tsay, S.-C., Wiscombe, W., and Laszlo, I.: DISORT, a general-purpose Fortran program for discrete-ordinate-method radiative
       transfer in scattering and emitting layered media: documentation of methodology, Tech. rep., Dept. of Physics and Engineering Physics,
805   Stevens Institute of Technology Hoboken, NJ 07030, 2000.

Stohl, A., Prata, A. J., Eckhardt, S., Clarisse, L., Durant, A., Henne, S., Kristiansen, N. I., Minikin, A., Schumann, U., Seibert, P., Stebel, K.,
       Thomas, H. E., Thorsteinsson, T., Tørseth, K., and Weinzierl, B.: Determination of time- and height-resolved volcanic ash emissions and

their use for quantitative ash dispersion modeling: the 2010 Eyjafjallajökull eruption, Atmospheric Chemistry and Physics, 11, 4333–4351, https://doi.org/10.5194/acp-11-4333-2011, 2011.

810 Thomas, G. E., Poulsen, C. A., Sayer, A. M., Marsh, S. H., Dean, S. M., Carboni, E., Siddans, R., Grainger, R. G., and Lawrence, B. N.: The GRAPE aerosol retrieval algorithm, Atmos. Meas. Tech., 2, 679–701, https://doi.org/https://doi.org/10.5194/amt-2-679-2009, 2009.

Van Eaton, A. R., Amigo, , Bertin, D., Mastin, L. G., Giacosa, R. E., González, J., Valderrama, O., Fontijn, K., and Behnke, S. A.: Volcanic lightning and plume behavior reveal evolving hazards during the April 2015 eruption of Calbuco volcano, Chile, Geophysical Research Letters, 43, 3563–3571, https://doi.org/10.1002/2016GL068076, 2016.

815 Vicente, G. A., Davenport, J. C., and Scofield, R. A.: The role of orographic and parallax corrections on real time high resolution satellite rainfall rate distribution, International Journal of Remote Sensing, 23, 221–230, https://doi.org/10.1080/01431160010006935, 2002.

Wang, C., Yang, P., Baum, B. A., Platnick, S., Heidinger, A. K., Hu, Y., and Holz, R. E.: Retrieval of Ice Cloud Optical Thickness and Effective Particle Size Using a Fast Infrared Radiative Transfer Model, Journal of Applied Meteorology and Climatology, 50, 2283–2297, https://doi.org/10.1175/JAMC-D-11-067.1, 2011.

820 Watts, P., Mutlow, C., Baran, A., and Zavody, A.: Study on cloud properties derived from Meteosat Second Generation observations, EU-METSAT ITT, 97, 181, 1998.

Watts, P. D., Bennartz, R., and Fell, F.: Retrieval of two-layer cloud properties from multispectral observations using optimal estimation, Journal of Geophysical Research, 116, D16 203, https://doi.org/10.1029/2011JD015883, 2011.

Wen, S. and Rose, W. I.: Retrieval of sizes and total masses of particles in volcanic clouds using AVHRR bands 4 and 5, Journal of Geophys-
825 ical Research, 99, 5421, https://doi.org/10.1029/93JD03340, 1994.

Western, L. M., Watson, M. I., and Francis, P. N.: Uncertainty in two-channel infrared remote sensing retrievals of a well-characterised volcanic ash cloud, Bulletin of Volcanology, 77, https://doi.org/10.1007/s00445-015-0950-y, 2015.

Wilkins, K. L., Mackie, S., Watson, M., Webster, H. N., Thomson, D. J., and Dacre, H. F.: Data insertion in volcanic ash cloud forecasting, Annals of Geophysics, https://doi.org/10.4401/ag-6624, 2015.

830 Wilkins, K. L., Watson, I. M., Kristiansen, N. I., Webster, H. N., Thomson, D. J., Dacre, H. F., and Prata, A. J.: Using data insertion with the NAME model to simulate the 8 May 2010 Eyjafjallajökull volcanic ash cloud, Journal of Geophysical Research: Atmospheres, 121, 306–323, https://doi.org/10.1002/2015JD023895, 2016.

Wilson, L., Sparks, R. S. J., Huang, T. C., and Watkins, N. D.: The control of volcanic column heights by eruption energetics and dynamics, Journal of Geophysical Research: Solid Earth, 83, 1829–1836, https://doi.org/10.1029/JB083iB04p01829, 1978.

835 Winker, D. M., Vaughan, M. A., Omar, A., Hu, Y., Powell, K. A., Liu, Z., Hunt, W. H., and Young, S. A.: Overview of the CALIPSO Mission and CALIOP Data Processing Algorithms, Journal of Atmospheric and Oceanic Technology, 26, 2310–2323, https://doi.org/10.1175/2009JTECHA1281.1, 2009.

Winker, D. M., Liu, Z., Omar, A., Tackett, J., and Fairlie, D.: CALIOP observations of the transport of ash from the Eyjafjallajökull volcano in April 2010, Journal of Geophysical Research: Atmospheres, 117, https://doi.org/10.1029/2011JD016499, 2012.

840 Yamanouchi, T., Suzuki, K., and Kawaguchi, S.: Detection of Clouds in Antarctica from Infrared Multispectral Data of AVHRR, Journal of the Meteorological Society of Japan. Ser. II, 65, 949–962, https://doi.org/10.2151/jmsj1965.65.6_949, 1987.

Yu, T., Rose, W. I., and Prata, A. J.: Atmospheric correction for satellite-based volcanic ash mapping and retrievals using "split window" IR data from GOES and AVHRR, Journal of Geophysical Research, 107, https://doi.org/10.1029/2001JD000706, 2002.

Zidikheri, M. J. and Lucas, C.: A Computationally Efficient Ensemble Filtering Scheme for Quantitative Volcanic Ash Forecasts, Journal of
845 Geophysical Research: Atmospheres, 126, https://doi.org/10.1029/2020JD033094, 2021.